

Article

Assessment of Saturation Effect on Hydraulic Fracturing in Sandstone and Thermally Treated Granite

Anna Shevtsova ^{1,*} , Sergey Stanchits ² , Egor Filev ¹, Tagir Karamov ¹, Vladimir Stukachev ¹ and Mikhail Spasennykh ¹

¹ Center for Petroleum Science and Engineering, Skolkovo Institute of Science and Technology, Bolshoy Boulevard 30, Bld. 1, 121205 Moscow, Russia; egor.filev@skoltech.ru (E.F.); t.karamov@skoltech.ru (T.K.); v.stukachev@skoltech.ru (V.S.); m.spasennykh@skoltech.ru (M.S.)

² Schmidt Institute of Physics of the Earth of the Russian Academy of Sciences, 123242 Moscow, Russia; s.stanchits@ifz.ru

* Correspondence: anna.shevtsova@skoltech.ru

Abstract: In this study, a set of laboratory experiments was carried out to study the parameters of hydraulic fractures induced in the dry and mineral-oil-saturated rocks and compare them with the geomechanical characteristics of tested samples. We chose sandstone and thermally treated granite as the materials for research. There are very few known studies related to the mechanical and acoustic properties of oil-saturated rocks, and even fewer studies describing, in detail, the parameters of hydraulic fractures generated in oil-saturated rocks. The hydraulic fracture parameters were determined using a set of independent sensors installed to measure the axial deformation of the sample (which is directly related to the aperture of created hydraulic fracture), fluid pressure, fluid volume injected into hydraulic fracture, and localization of acoustic emission (AE) events, generated during the propagation of hydraulic fractures. Our study focuses on the investigation of the influence of rock properties, altered by mineral oil saturation and thermal treatment, on such parameters of hydraulic fracturing as breakdown pressure (BP), fracture aperture, and the resulting roughness of the hydraulic fracture surface. In addition, we studied the influence of injected fluid viscosity on the parameters of created hydraulic fractures. It was revealed that the saturation state caused a reduction in the values of mechanical parameters such as Young's modulus, compressive strength, and cohesion, and had a similar reducing influence on the breakdown pressure. The values of HF parameters, such as fracture width and the volume of fracturing agent injected into the HF, are higher in the tests for both saturated sandstone and saturated TT granite. However, we found out that thermal treatment of granite samples led to a much more significant reduction in the values of mechanical and acoustic parameters than the mineral-oil saturation procedure because it created a dense network of thermally induced cracks. The results obtained in our laboratory studies can be taken into account in the modeling of hydraulic fracturing in the field.

Keywords: hydraulic fracturing; acoustic emission; sample saturation; fracturing fluid viscosity; fracture propagation; fracture surface; P-wave velocity



Citation: Shevtsova, A.; Stanchits, S.; Filev, E.; Karamov, T.; Stukachev, V.; Spasennykh, M. Assessment of Saturation Effect on Hydraulic Fracturing in Sandstone and Thermally Treated Granite. *Minerals* **2023**, *13*, 777. <https://doi.org/10.3390/min13060777>

Academic Editor: Pieter Bertier

Received: 4 May 2023

Revised: 23 May 2023

Accepted: 31 May 2023

Published: 6 June 2023



Copyright: © 2023 by the authors. Licensee MDPI, Basel, Switzerland. This article is an open access article distributed under the terms and conditions of the Creative Commons Attribution (CC BY) license (<https://creativecommons.org/licenses/by/4.0/>).

1. Introduction

Hydraulic fracturing is known as the main method of stimulating oil and gas production, when the injection of a mixture of water and chemicals into a reservoir generates a network of fractures, enhancing hydrocarbon production [1–3]. Complex fracture networks are formed by the reactivation of natural fractures and creation of new fractures [4]. In addition, hydraulic fracturing is applicable to the development of an enhanced geothermal system (EGS) [5,6].

Despite the widespread implementation of hydraulic fracturing and the promising results of stimulated oil and gas production, the procedure still remains challenging, expensive, and the stimulation may be short-lasting. Due to the varied and unique mechanical

characteristics of the rock, the geological conditions, and the in situ stress states of each reservoir, field studies of hydraulic fracturing have become rather complicated. Furthermore, the geological structure of an unconventional reservoir significantly influences the features of reservoirs. In recent years, unconventional tight sandstone reservoirs with low permeability have been developed, and a significant number of horizontal wells have been drilled for multi-stage hydraulic fracturing, to enhance production from the reservoirs [7,8].

As shown earlier, some factors, such as pre-existing natural cracks, bedding planes, and clay content, can have a significant impact on the efficiency of hydraulic fracturing operations [9–11], and they must be taken into account while modeling the process. That is why laboratory experiments can be considered a necessary part of hydraulic fracturing research, since they can be controlled and reproduced using core samples obtained from reservoirs [12]. In addition, laboratory experiments are widely used as an excellent method for verifying the accuracy of numerical simulation results [13].

Numerous studies have examined the effect of water on the mechanical properties of rocks, and it has been observed that water reduces the compressive strength, tensile strength, elastic modulus, and cohesion of the rocks; however, the plastic behavior of rocks is enhanced. The percentage reduction in compressive strength varies from one type of rock to another and may be up to 90% in saturated mudstone [14], up to 29% in saturated marble [15], up to 88% in saturated tuff [16], and up to 40% in sandstone [17]. Several potential mechanisms, including clay mineral softening, the friction weakening effect, and the influence of pore water pressure have been proposed as the main cause for the observed reduction in strength mentioned above [18,19].

Furthermore, not only the mechanical properties of the rock but also the acoustic properties change in the saturated state. The effect of saturation on the compressional wave velocity has been studied in many papers, demonstrating that higher values of P-wave velocities were observed for the saturated samples and lower values were observed for the dry samples (e.g., Boulanouar et al. [20]). The values of shear wave velocities in a wet, porous material will always be lower than those in the dry material [21]. In addition, P-wave velocities for wet rocks may be calculated on the basis of a P-wave velocity value for dry rocks [22]. However, saturation of the sample aggravates attenuation and scattering of elastic waves. Johnston et al. [23] concluded that the friction of thin cracks and grain boundaries is the primary reason for seismic attenuation, and the presence of a fluid will wet the grain boundaries and crack surfaces.

Microseismic observation of hydraulic fractures in formations provides insights into the fracture growth; however, quantitative microseismic interpretation is often challenging due to limited data on reservoir characteristics affected by in situ stresses and pre-existing fractures. Meanwhile, hydraulic fracturing in the laboratory can be used to characterize the geometry of fractures that occur under different conditions (e.g., stress state) [24]. Reliable assessment of the characteristics of created hydraulic fractures, such as fracture geometry, surface roughness, etc., in field conditions is a very complicated task, while the geometrical characteristics of created hydraulic fractures can be directly determined in a laboratory test, e.g., by computed tomography [25] or by laser scanning technique [26]. Knowledge of the roughness and the aperture of the created hydraulic fractures is crucial for arranging successful proppant delivery. However, in the field, the aperture of hydraulic fractures can be estimated very roughly, while in the laboratory it is possible to directly measure the deformation of the sample related to the opening of hydraulic fractures [25,27]. Similarly to microseismicity recorded in the field, acoustic emissions (AE) can also be monitored in the laboratory using sensitive, high-frequency data acquisition systems [28].

Almost all reservoirs contain natural fractures [29,30], and the presence of natural fractures, as well as bedding planes, has a significant impact on the hydraulic fracture propagation [31]. In order to enhance the productivity of a low-permeability formation, complex fracture networks should be induced, which are often formed by reactivated natural fractures and newly created fractures [4]. This produces a large stimulated reservoir volume (SRV). However, due to the complex morphology of an induced fracture network,

it is important to assess fracture roughness for proper proppant distribution, slowing down the rate of hydraulic fracture closure, and improving effective fracture conductivity [32].

Since there are relatively few studies related to the characteristics of oil-saturated rocks, mechanical and acoustic properties, as well as hydraulic fracture parameters of oil-saturated rocks remain poorly understood. We also emphasize the importance of pre-existing microcracks in granite in the process of hydraulic fracturing. Our study focuses on laboratory observations of hydraulic fractures created in the dry and mineral-oil-saturated specimens of sandstone and thermally treated (TT) granite, to explore the effect of oil saturation and fracturing fluid viscosity on mechanical properties, which, in turn, affect the parameters of the created hydraulic fractures and associated AE. A series of confined multistage tests were conducted to determine the mechanical properties of original, thermally treated, and oil-saturated specimens. In addition, hydraulic fracturing tests were conducted using a set of independent sensors to register the sample deformation, directly related to the hydraulic fracture aperture, as well as fracturing fluid pressure and acoustic emission (AE) activity.

2. Materials and Methods

2.1. Experimental Setup

The experiments were conducted in the pseudo-triaxial cell of the MTS-815 loading frame (Figure 1a) manufactured by the Material Testing Systems Corporation, where constant axial and confining pressures were maintained during the hydraulic fracturing induced by fluids injected into the specimen. The parameters of the hydraulic fracture growth were recorded by three independent systems: (1) the set of acoustic emission (AE) sensors, glued to the cylindrical surface of the specimen (Figure 1b, green rectangle); (2) the extensometer used to measure the deformation of the specimen in the axial direction (Figure 1b, pink rectangle), and (3) the sensors recording the pressure and volume of the injected fluid. The combination of data obtained from independent systems allows us to reliably determine the moment of fracture initiation, to estimate the speed of hydraulic fracture propagation, and to measure the specimen deformation related to the opening of the hydraulic fracture. After the test, the geometry of the created hydraulic fracture and the roughness of the hydraulic fracture surface were characterized using a laser scanning technique.

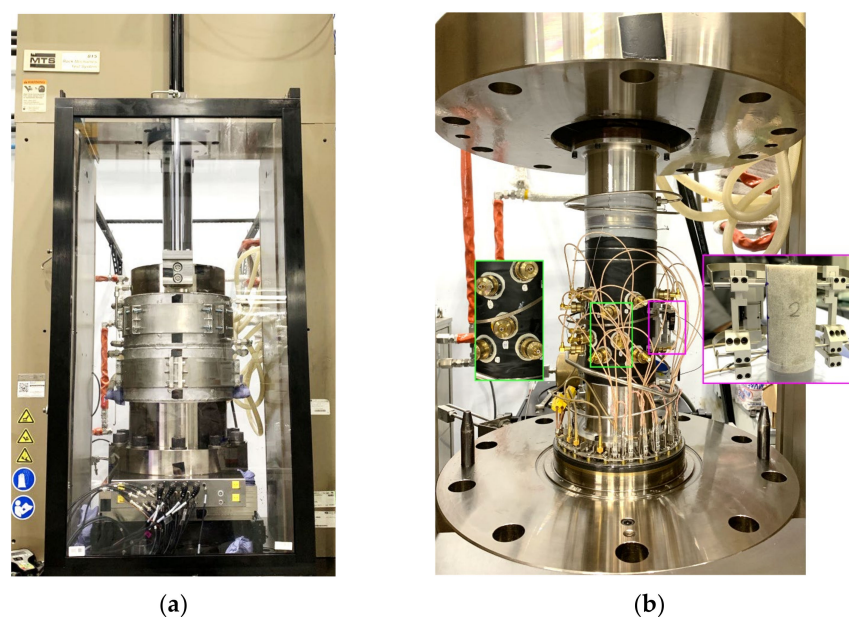


Figure 1. (a) General view of the MTS 815 servo-hydraulic unit with a downturned chamber; (b) installation diagram of the axial extensometer (pink rectangle) and the brass housings of the acoustic emission sensors glued to the sample (green rectangle).

The sample preparation procedure included the cylindrical specimens coring and grinding the end surfaces of the specimens with a diamond grinding disk to a flatness deviation of no more than 0.03 mm. After that, a wellbore of 8 mm diameter and 60 mm length was drilled in the center of the specimen, and the metal casing was glued into the wellbore in such a way as to leave an uncased open-hole section of the rock of 6 mm length (Figure 2). To simulate the perforation and to specify the direction of fracture development, a transverse notch was cut 2–3 mm deep in the center of the open-hole section. Before the sample was installed into the pseudo-triaxial cell, it was sealed with the oil-resistant jacket separating the confining oil from the sample. The final stage of the sample preparation procedure was gluing a set of 18 AE sensors to the cylindrical surface of the sample.

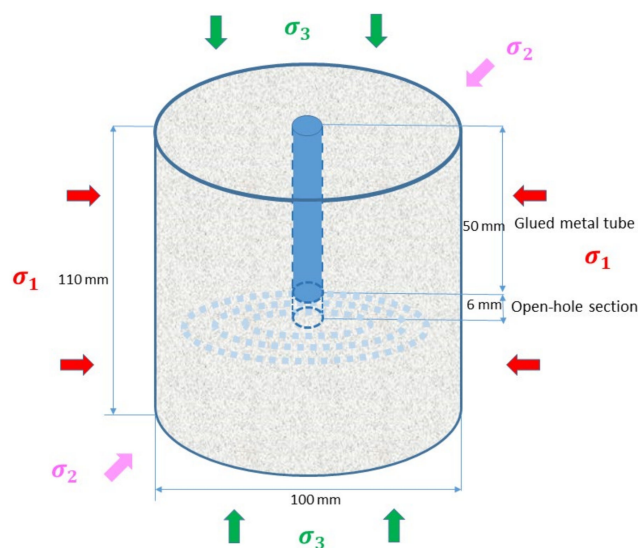


Figure 2. Sample loading diagram in the pseudo-triaxial chamber: $\sigma_1 = \sigma_2 > \sigma_3$.

In the pseudo-triaxial loading frame, two out of the three principal stresses must be equal, and we chose the loading scheme when the maximum and medium stresses were applied to the cylindrical surface of the rock (Figure 2). The samples were initially loaded hydrostatically to a stress state, where $\sigma_1 = \sigma_2 = \sigma_3 = 22$ MPa were applied to the sample, and then σ_3 , applied along the cylinder axis, was decreased to 8 MPa. This loading scheme allows the study of the initiation of hydraulic fracture growth in the direction perpendicular to the minimal applied stress σ_3 (Figure 2), while $\sigma_1 = \sigma_2 = 22$ MPa were applied to the cylindrical surface of the rock. It should be noted that with this loading scheme, the borehole is drilled in the direction of minimum principal stress, and laboratory hydraulic fracturing can simulate a horizontal well in the field drilled in the σ_h direction. The sample expands in the vertical direction, and the sample deformations associated with the opening of the HF were precisely measured by a vertical extensometer installed on the cylindrical surface of the sample.

In addition, during our experimental study, Newtonian viscous silicone oil (SO) with viscosities of 1000 cP, 10,000 cP, and 100,000 cP and non-Newtonian OilGel 40/40 (OG) with a viscosity decreasing from 1220 cP at 100 rpm to 310.81 cP at 300 rpm (a detailed description of which was published in [25]) were injected into the specimens to induce a hydraulic fracture. Mineral oil Multitherm PG-1 (with a viscosity of 46 cP) was used as a fluid for the saturation of samples in the pseudo-triaxial cell. Initially, a confining pressure of 2 MPa was applied to the tested specimen, then a vacuum was applied to the sample for at least one hour to remove the air trapped in the open pore space. Thereafter, a constant pore pressure of 1 MPa was applied to saturate the sample. The mineral oil Multitherm PG-1 was used for the sample saturation to avoid additional effect of clay swelling in sandstone. Moreover, the properties of the mineral oil were fully investigated [33]. Additionally, the sample saturation was confirmed by P-wave velocity measurements along the different ultrasonic transmission traces.

2.2. The Fracture Surface Scanning

After the tests, the obtained hydraulic fracture surfaces were scanned by an EinScan HX handheld 3D scanner (Shining 3D). A hybrid blue laser and LED light source were integrated into the scanner to increase the efficiency and reliability of the results (Figure 3a). The high resolution of the images is provided by the minimum point distance of 0.05 mm and the accuracy is up to 0.04 mm [34]. Analysis of the obtained images of hydraulic fracture surfaces (Figure 3b) allows the calculation of the roughness and tortuosity of the fracture surfaces.

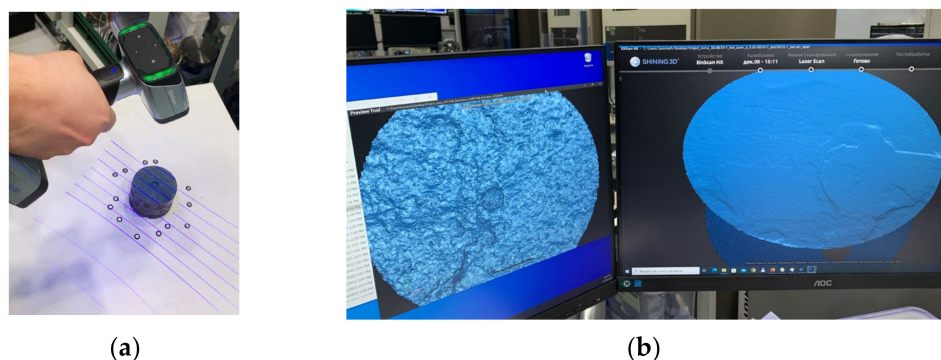


Figure 3. (a) The EinScan HX handheld 3D scanner (Shining 3D) [35]; (b) the images of the sample surfaces.

2.3. Specimens Description

For our experimental research, three types of rocks were tested: sandstone, unheated granite, and thermally treated (TT) granite. Their descriptions are presented in the following subsections.

Sandstone

Tested samples of sandstone were obtained from the Prirakhtovskoye field (Omsk region, Russia) (Figure 4). They were taken from a depth of 2426.35–2428.75 m. The cylindrical samples with a diameter of 77 mm and a length of 105 mm were prepared for laboratory fracturing experiments. Moreover, four cylindrical samples with a diameter of 30 mm and a length of 60 mm were prepared for the multi-stage triaxial compression (MTXC) tests.



Figure 4. The schematic location map of the Prirakhtovskoye field (Omsk region, Russia).

The studied sandstone is a light-grey, fine-grained sedimentary rock. The size of sandstone grain is up to 0.5 mm. It consists of rounded fine grains of silica (quartz) that are all of the same size, and it is cemented by clay. It consists of quartz, albite, kaolinite, illite, and chlorite group. The mineral composition of the samples was analyzed with the X-ray powder diffraction technique on the Huber G670 diffractometer. The composition of the sandstone is shown in Figure 5. Sandstones are composed of quartz predominantly. Clay minerals are represented by illite, kaolinite, and chlorite.

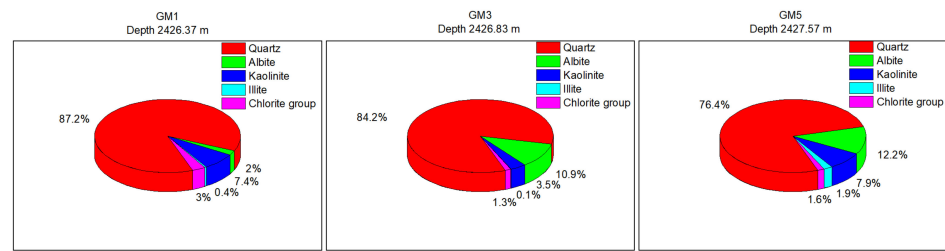


Figure 5. The results of the XRD analysis of the sandstone samples.

The main sandstone properties are listed in Table 1. The average value of Young’s modulus of the samples drilled perpendicular to the formation’s layers is 13.61 GPa, and the average value of Young’s modulus of the samples drilled parallel to the formation’s layers is 16.87 GPa. The second value is 19% higher than the first one, and it was calculated by Equation (1). The differences between the other geomechanical parameters are 2%, 15%, 10%, and 5% for Poisson’s ratio, compressive strength, cohesion and friction angle, respectively.

$$c = \frac{a - b}{b} \times 100, \% \tag{1}$$

Table 1. Summary of the mechanical characteristics of the sandstone samples.

Parameter	Unit	Range	a *	Range	b **	c, %
Depth interval	m	2426.48–2428.82	-	2426.54–2427.58	-	-
Density ρ	g/cm ³	2.23–2.32	2.271	2.23–2.32	2.269	0.01
Young’s modulus E	GPa	12.45–14.80	13.61	16.03–17.71	16.71	19
Poisson’s ratio ν	-	0.08–0.12	0.101	0.08–0.12	0.099	2
Compressive strength	MPa	151.12–175.06	161.78	127.65–160.41	141.25	15
Cohesion C	MPa	13.70–18.80	16.28	12.20–17.40	14.80	10
Friction angle φ	°	35.5–36.5	35.88	33.10–35.20	34.15	5

*—the samples were drilled perpendicular to the formation’s layers; **—the samples were drilled parallel to formation’s layers.

Unheated granite and Thermally Treated (TT) Granite

The Tashmurunsky granite quarry is located in the Republic of Bashkortostan, Russia. The rock was cut out from the rock formation without the use of explosives, so we expected a low density of pre-existing cracks in the original samples. Tashmurunsky granite is an almost homogeneous igneous rock of light-gray color with a fine-medium-grained structure. The size of granite grain is 3–5 mm. The mineral composition was determined as follows: quartz—29%, microcline—40%, plagioclase—25%, biotite—5%, and other—1%. A comparison of the photos of the unheated and TT granites is shown in Figure 6.

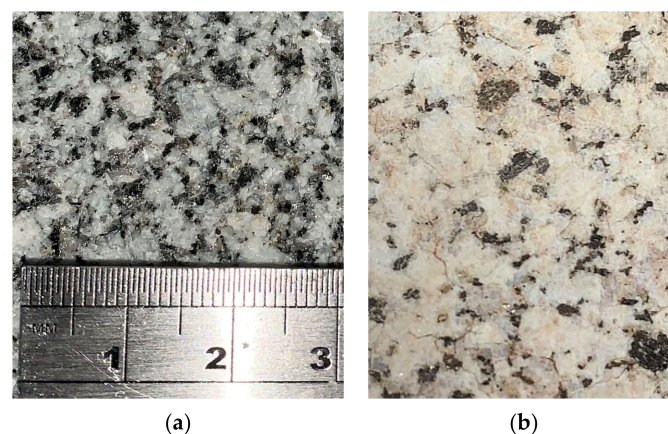


Figure 6. The photos of Tashmurunsky granite samples: (a) unheated sample; (b) thermally treated at 800 °C sample.

The thermal treatment was applied to the granite sample to create artificially fractured material to study the process of the fracture initiation and propagation in the highly fractured rock matrix. The properties of the unheated and TT granite samples are listed in Table 2.

Table 2. Comparison of properties of the unheated and thermally treated granites.

	Unheated	Thermally Treated	Thermally Treated
	Dry	Dry	Saturated
Porosity, %	1.10	3.97	3.97
Gas permeability, mD	0.01	9.13	9.13
Young's modulus E, GPa	62.55	21.28	18.24
Poisson's ratio ν	0.18	0.10	0.06
Compressive strength, MPa	447.62	389.13	333.20
Cohesion C, MPa	24.4	15.6	13.8
Friction angle φ , °	57.0	58.0	56
Tensile strength, MPa	5.50	1.84	-
P-wave velocity at $P_c = 20$ MPa, m/sec	4800	2300	3800

Cylindrical specimens with the following dimensions were prepared for testing: a diameter in the range of 99–102 mm and a length of 115–116 mm. At room temperature, the average density of the tested unheated granite is 2.70 g/cm³ and for the dry TT granite, it is 2.50 g/cm³. The P-wave velocity is 4800 m/s for unheated granite and 2300 m/s for the dry TT granite.

2.4. Heating Procedure

High-temperature heating was used to create a dense network of cracks in the Tashmurunsky granite. Based on the previous publication [36], it is known that the development of intra-granular cracks begins at temperatures above 573 °C, due to the α - β transition of quartz grains. Before the experiments, the granite samples were heated to 800 °C with a constant heating rate of 2.77 °C/min (Figure 7a). It was shown in [37] that the choice of a constant heating rate of less than 5 °C/min enables the avoidance of possible thermal shock to the rock. The samples were then kept at the target temperature (800 °C) for 3 h, and afterwards, slowly cooled to room temperature in a natural way after turning off the furnace. A high-precision, electric, fiber-insulated chamber furnace SNOL 30/1300 was used to heat the samples (Figure 7b).

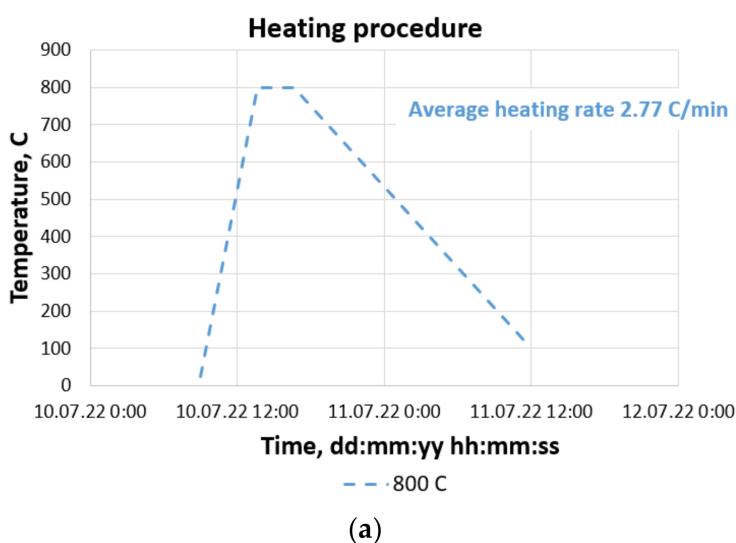


Figure 7. (a) Heating history graph of the Tashmurunsky granite thermal treatment process; (b) high-accuracy, electric, fiber-insulated chamber furnace SNOL 30/1300.

3. Results

3.1. Mechanical Characteristics of Dry and Mineral-Oil-Saturated Sandstone Specimens

This part of the experiments aimed to examine the mechanical properties of dry (Figure 8a) and fully mineral-oil-saturated (Figure 8b) sandstones. The multi-stage tests were conducted at the following confining pressure levels: 8.55; 17.1; 25.65; and 34.2 MPa. The confining pressure values were calculated using the actual formation pressure measurements.

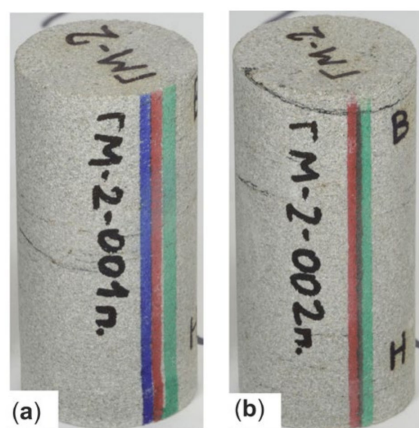


Figure 8. Photos of samples before the experiments: (a) dry GM2-001 and (b) mineral-oil-saturated GM2-002.

The main parameters of the studied sandstone specimens are shown in Table 3. As noted earlier, the density, effective porosity, and gas permeability of the sample, GM2-002, were measured before the saturation procedure. The values of density, effective porosity, and gas permeability were 0.01%, 2%, and 14% higher, respectively, for the GM2-002 sample, so these samples can also be considered «twins».

Table 3. General information about tested sandstone samples.

Sample Id		Length	Diameter	Weight	Density	Porosity	Gas Permeability
-	-	mm	mm	g	g/cm ³	%	mD
GM2-001	Dry	59.69	29.03	91.531	2.32	12.46	0.59
GM2-002	Saturated	60.99	29.03	93.647	2.32	12.69	0.68

The mineral-oil-saturated specimen has 2% lower Young's modulus, 5% lower compressive strength, and 7% lower cohesion and 14% higher P-wave velocity than the dry specimen (Table 4). Thus, mineral oil saturation also affects sandstone's mechanical properties.

Table 4. Comparison of properties of the dry (GM2-001) and mineral-oil-saturated (GM2-002) sandstone specimens.

	GM2-001	GM2-002
Young's modulus E, GPa	14.36	14.13
Poisson's ratio ν	0.10	0.09
Compressive strength, MPa	175.06	166.67
Cohesion C, MPa	18.8	17.6
Friction angle φ , °	36.5	36.0
P-wave velocity at $P_c = 8.55$ MPa, m/sec	3649	4250

3.2. Hydraulic Fracture Propagation in Sandstone

Hydraulic fracturing experiments were conducted on the four sandstone specimens at σ_1 of 22 MPa and σ_3 of 8 MPa. The horizontal fracture orientation was induced and controlled by the sample loading scheme; in all tests, the induced fracture was oriented in the σ_1 direction perpendicular to the σ_3 direction. Fluids such as non-Newtonian OilGel 40/40 (OG with a viscosity equal to 1220 cP at 100 rpm, which decreases to 310.81 cP at 300 rpm) and Newtonian viscous silicone oils (SOs with viscosities of 10,000 cP and 100,000 cP) were injected at a constant rate of 5 mL/min. The main experimental conditions are described in Table 5.

Table 5. Relevant information about the hydraulic fracturing experiments in sandstone specimens.

Sample Id	σ_1	σ_3	Fracturing Fluid	Injection Flow Rate	Saturation
-	MPa	MPa	-	mL/min	-
GM4-101	22	8	OG	5	saturated
GM5-101	22	8	SO 10,000	5	saturated
GM6-102	22	8	OG	5	dry
GM7-101	22	8	SO 100,000	5	saturated

Figure 9 indicates a set of parameters recorded during the hydraulic fracturing of sandstone samples (GM5-101 and GM7-101) by a few independent observation systems. Figure 9a shows the wellbore pressure (red) approaching a maximum value of 49.8 MPa at 186.0 s and the cumulative number of localized acoustic emission (AE) signals (purple) that demonstrated slight acceleration at 185.5 s, or about half a second before the wellbore pressure approached the maximum value (the breakdown moment) in the test GM5-101. In contrast to the test GM5-101, the injection of more viscous fracturing fluid caused a slightly higher maximum value of wellbore pressure (red) which was equal to 53.1 MPa, and the initiation of acoustic emission (AE) signals (purple) was approximately one second before the breakdown moment in the test GM7-101. Specimen deformation was measured by two extensometers, labeled Ext_A (Figure 9b,j, blue) and Ext_B (Figure 9b,j, red), mounted opposite each other on the cylindrical surface of each specimen. During hydraulic fracturing, all stresses applied to the specimens were kept constant, and the LVDT sensor measured the position of the piston, maintaining a constant stress σ_3 applied in the vertical direction (Figure 9b,j, green). The deformations measured in the tests GM5-101 and GM7-101 (Ext_A, Ext_B and piston displacement, Figure 9b,j) indicate the initiation of HF at approximately the same time as the increase in AE activity (Figure 9a,i). Note that all three deformations were measured independently by three sensors, and their values coincide within 10% of the difference. Such close correspondence of the experimentally measured values allows us to conclude that, first of all, the deformation of the sample is directly related to the opening of the hydraulic fracture confirmed by the onset of AE. Secondly, the close coincidence of the deformations measured on the opposite sides of the specimens (Ext_A and Ext_B) may indicate the symmetrical opening of the created hydraulic fracture.

The entire volume of injected fluid can be divided into two components: a linearly increasing fluid volume, which is associated with the compressibility of the rock and fluid, the elastic expansion of the hydraulic injection system due to the pressure increase, and a non-linearly rising fluid volume associated with the cracks-and-pores-filling processes during the propagation of the hydraulic fracture [27,38]. Figure 9c,k shows the fluid volume having entered the fracture; this calculated parameter was obtained as a subtraction of the linearly rising component of the fluid volume from the total fluid volume injected into the wellbore. Note that the onset of fluid volume increase in Figure 9c,k corresponds very closely to the independently measured onset of displacements in Figure 9b,k and the cumulative AE number curve in Figure 9a,i, purple.

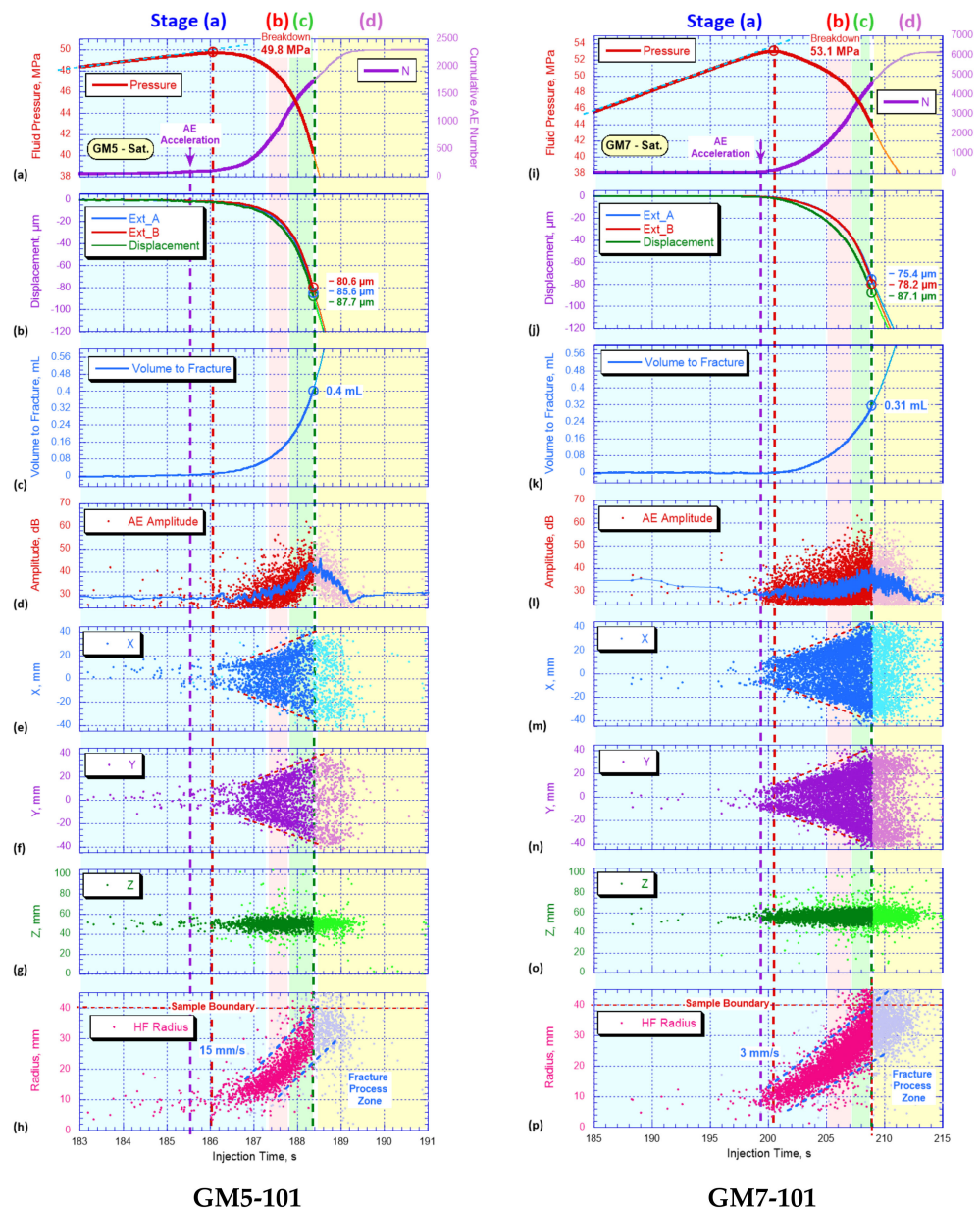


Figure 9. (a,i) Fluid pressure (red) and the total number of localized AE signals (purple); (b,j) axial deformations measured by the left (Ext_B, red) and right (Ext_A, blue) extensometers and a curve demonstrating the piston position (green); (c,k) the volume of fluid injected into the hydraulic fracture; (d,l) amplitudes of AE signals; (e,f,m,n) horizontal coordinates of the located AE signals in the X and Y directions, respectively; (g,o) vertical coordinates Z of the localized AE signals; (h,p) distribution of the distances between the located AE signals and the axis of the sample. All parameters are plotted versus the time of sample testing.

The remaining four graphs (d–h and l–p) in Figure 9 show the AE parameters recorded during the test. Each magenta dot in Figure 9d,l shows the amplitude of the localized AE signal in dB scale, and the blue line in Figure 9d,l shows the amplitudes smoothed in the sliding window of 25 signals. An increase in the AE signal amplitudes can be seen shortly after the initiation of the HF, which we associate with the enlargement of the microcracks. The plots in Figure 9e–f,m–n show the positions of the XY coordinates of the localized AE events along the horizontal axis of the sample, and in Figure 9g,o the vertical coordinate along the Z axis of the sample. One can see a very symmetrical propagation of the AE cloud along the horizontal X and Y coordinates (Figure 9e–f,m–n), while, along the vertical

Z direction, most of the AE events are localized within a zone of about 20 mm thickness (Figure 9g,o). The distances between the wellbore (or the sample center) and each located AE event are presented in Figure 9h,p, indicating an increase in the radius of the created hydraulic fracture.

It can be seen that the front of the HF propagates toward the sample boundary at a rate of approximately 3 mm/s and 15 mm/s in the tests GM5-101 (Figure 9h, upper dashed blue line) and GM7-101 (Figure 9p, upper dashed blue line), respectively. This considerable difference in fracture propagation rates was caused by the 10-fold difference in the viscosity values of injected SOs. Note the existence of the rear front of the propagating hydraulic fracture (Figure 9h,p, lower dashed blue line), indicating the approximately 20-mm-wide radiation of induced AE events within the fracture process zone (FPZ). A detailed description of the AE localization technique is presented in [27,38]; the accuracy of the AE event localization in our study was about 5 mm. The position of the sample boundary is indicated by the horizontal red dashed line in Figure 9h,p, and it can be seen that the fracture front reached the sample boundary at approximately 188.4 s and 209.0 s in the tests GM5-101 and GM7-101, respectively, which is indicated by the vertical dashed blue line in Figure 9. Note that this moment corresponds to the maximal value of the AE amplitude (Figure 9e,m). A similar correlation of the registration of the maximal value of the AE amplitudes with HF approaching the sample boundary was observed in [27]. The entire process of HF propagation up to the sample boundary was divided into three consecutive time intervals, providing an equal number of 576 AE signals for each stage, labeled stage (a), (b), and (c) in Figure 9. The very last stage (d) in Figure 9 (highlighted by the yellow rectangle) indicates 584 AE signals localized after the moment when the front of the FPZ approached the sample boundary. The analysis of the results presented in Figure 9 shows that at the moment marked by the vertical dashed line, the displacements in the range of 80.6–87.7 μm and 75.4–87.1 μm were recorded in the tests GM5-101 (Figure 9b) and GM7-101 (Figure 9j), respectively. Additionally, 0.4 mL of 10,000 cP SO and 0.31 mL of 100,000 cP SO were injected into the fracture in the tests GM5-101 (Figure 9c) and GM7-101 (Figure 9k), respectively. These values, experimentally determined by a few independent sensors, can be used for verification of the radial hydraulic-fracture-propagation models.

Three orthogonal projections of the coordinates of localized AE events are shown in three rows in Figure 10, divided into four columns corresponding to the consecutive time intervals indicated in Figure 9 as stages (a) through (d). The spheres depicted in Figure 10 represent the positions of the AE signals in three-dimensional space; the color of the spheres corresponds to the time scale shown on the color bar placed at the bottom of the lower row of projections. The diameter of the spheres is proportional to the magnitude of the AE signals, calculated as a logarithm of the recorded AE amplitude. The top view of the orthogonal projections of the AE signal distributions demonstrates the radial shape of the FPZ propagation (Figure 10, upper row). The locations of the AE events exactly replicate the shape of the fractures obtained in all the tests performed. Note that in case of high-viscosity fluid injection, the existence of a lag between the fracture process zone (FPZ) and the fluid front was experimentally confirmed [39]; however, taking into account the symmetry of the deformation measured on the sample boundary, one can assume that the fluid front also propagates radially in the GM5-101 and GM7-101 tests.

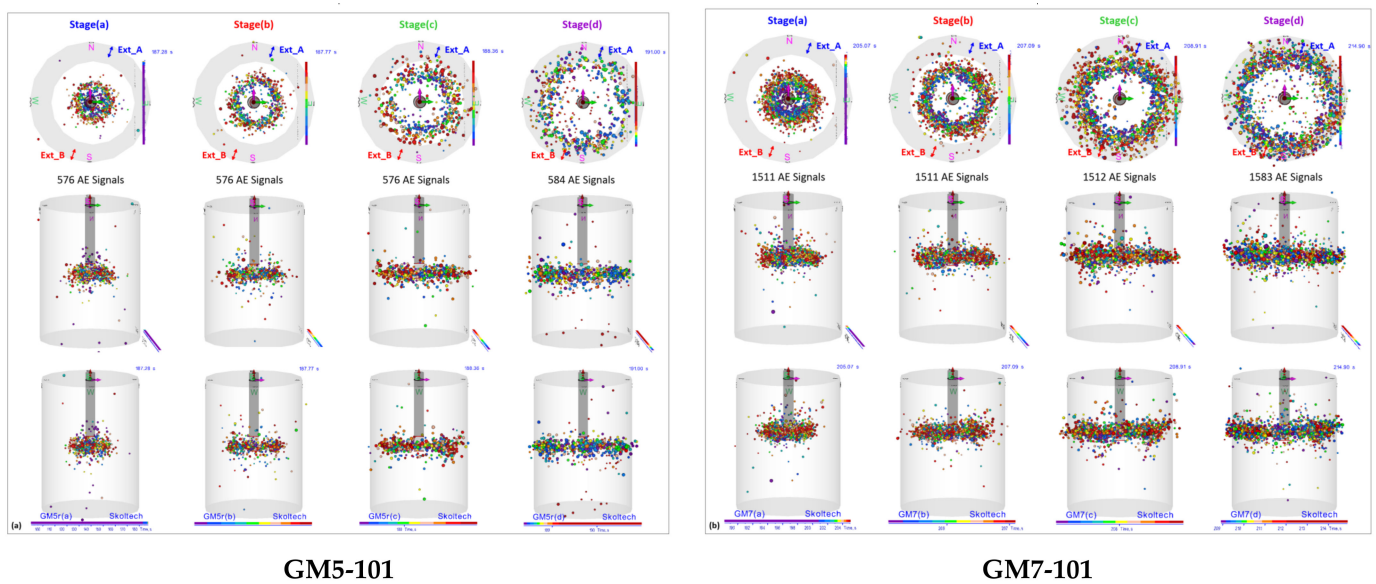


Figure 10. Three orthogonal projections of the AE signal positions within the GM5-101 (a) and GM7-101 (b) samples, hydraulically fractured by high-viscosity SO injections (10,000 cP for GM5-101 and 100,000 cP for GM7-101).

In the previous test, hydraulic fracturing was induced by the injection of high-viscosity silicone oil; however, in the field, fluids with significantly lower viscosities are usually used. Therefore, in the next two tests, we studied the fracturing of similar sandstone samples, but induced it by injecting diesel-based fluid OG 40/40, which is specially designed for hydraulic fracturing in the field. Sample GM6-102 was tested in dry conditions, and sample GM4-101 was saturated with mineral oil before the fracturing. The test results are shown in Figure 11. The reason for saturating the specimen is based on the fact that in nature, most of the rocks in a reservoir are saturated with a formation fluid. The fracture parameters were determined at the moment when the fracture approached the sample boundary, based on the analysis of the AE results. In order to determine this moment with the highest possible accuracy, combined criteria were applied, based on the analysis of spatial distributions of the AE signals (Figure 11h,p) (indicating the appearance of the AE signals in the vicinity of the sample boundary), and AE amplitudes approaching the maximum values (Figure 11d,l) (indicating the appearance of the largest microcracks) were used. It should be noted that, with the loading scheme used (Figure 2), the minimum principal stress was applied in the vertical direction and was kept constant during the stages of fluid injection and propagation of hydraulic fracture. However, during the very fast HF propagation, the massive piston of the loading frame could not adjust its position in order to maintain constant σ_3 stress. As a result of piston inertia, some increase in the minimum principal stress was recorded, occurring mainly after the HF approached the specimen boundary. For all analyzed tests, it was specifically verified that, at the moment when HF approached the cylindrical surface of the rock, the minimum principal stress increased by less than 10%. According to the parameters shown in Figure 11, the saturated sample (GM4-101) is characterized by a 13% lower BP and a 70% larger sample deformation than the dry sample (GM6-102). The maximum value of the AE amplitudes is also slightly lower in the saturated sample. Although the same fluid was injected into the dry and saturated specimens, the saturated specimen (GM4-101) demonstrates a larger volume having entered the fracture (Figure 11k), a larger axial deformation of the specimen caused by the fluid-driven HF opening (Figure 11j), and a slower speed of HF propagation (Figure 11p).

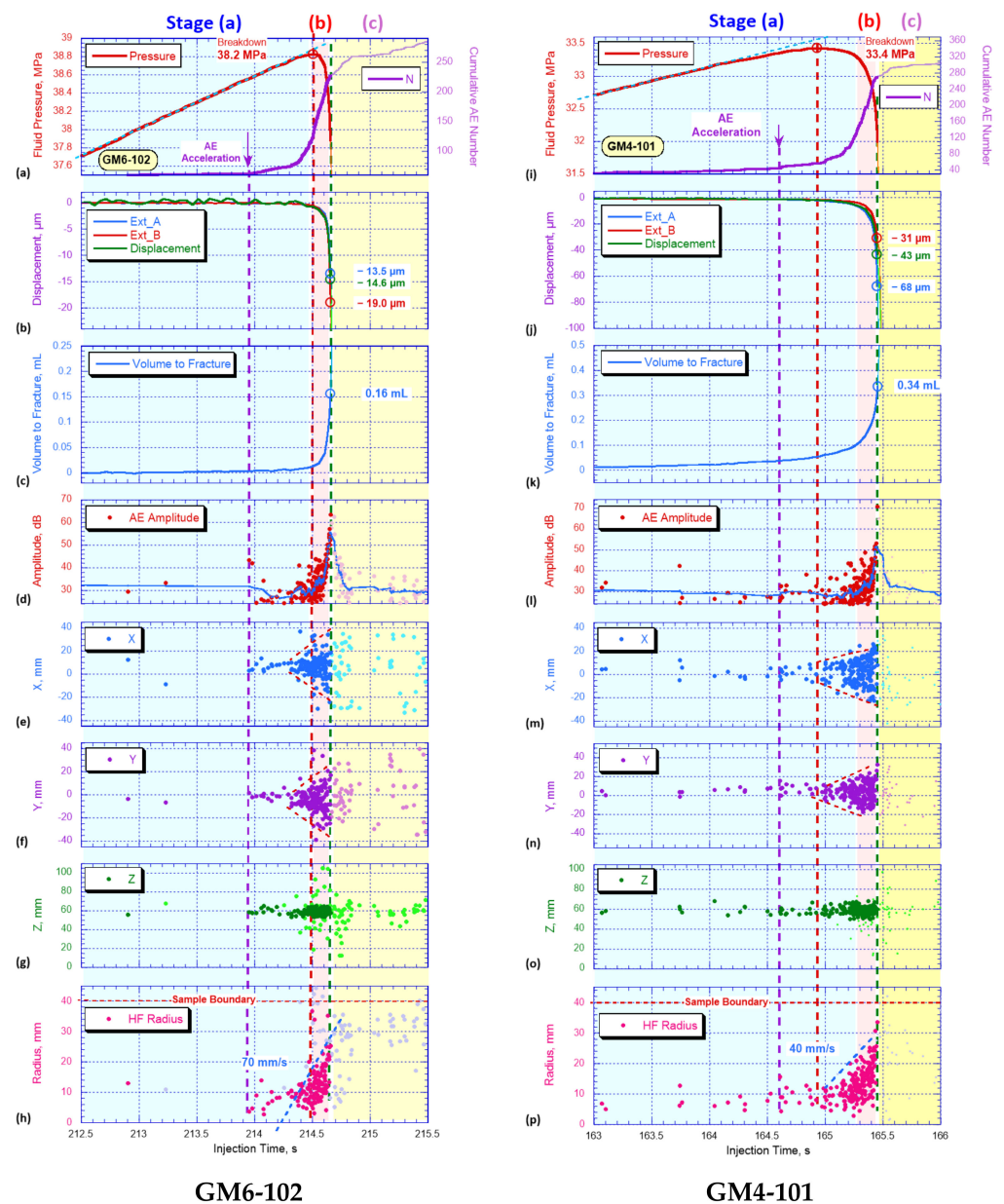


Figure 11. (a,i) fluid pressure (red) and total number of located AE signals (purple); (b,j) axial deformations measured by the left (Ext_B, red) and right (Ext_A, blue) extensometers and a curve demonstrating the piston position (green); (c,k) the volume of fluid injected into the hydraulic fracture; (d,l) amplitudes of AE signals; (e,f,m,n) horizontal coordinates of the located AE signals in the X and Y directions, respectively; (g,o) vertical coordinates of the localized AE signals; (h,p) distribution of the distances between the located AE signals and the axis of the sample. All parameters are plotted versus the time of sample testing.

Moreover, the influence of the fluid viscosity on fracture parameters can be analyzed by comparing the experimental results recorded with the injection of OG (GM4-101) and viscous SO (GM5-101) demonstrated above. Pumping less viscous OG induces the fracture at a 33% lower BP and with an almost 40% smaller sample deformation, related to HF aperture. In addition, the fracture induced by injecting less viscous fluid propagates almost five times faster in dry sandstone, and almost three times faster in saturated sandstone than the fracture driven by injecting SO into the saturated sandstone specimen (Figure 9p) shown above.

Figure 12 depicts the three-dimensional spatial distribution of the AE signals recorded during the three experimental stages for the dry sample (GM6-102) and the saturated sample (GM4-101). The middle column, labeled stage (ab), shows all AE events localized from the HF initiation to the moment when the HF approached the cylindrical surface of the rock. As it was shown above, this moment also coincides with the moment of maximal AE amplitude registration (Figure 11d,l). The left column of plots, labeled stage (a), shows the initial part of the HF propagation up to the moment when half of the number of the AE signals localized before the HF approached the surface of the rock, was recorded. Most of the AE signals recorded during stage (a) were localized near the open-hole section, with small asymmetry indicating the preferred direction of the initial stage of the HF propagation. In contrast to the almost symmetrical fracture growth in the dry sample (GM6-102), the fracture development in the saturated sample (GM4-101) shows significant asymmetry based on the results of measurements recorded by two observation systems. According to the located AE events, the fracture growth significantly prevails in the north-east direction, or in the direction of the installation site of the axial extensometer, labeled Ext_A (Figure 12b, upper row, blue). The results presented in Figure 11j (GM4-101, right column of plots) show that the deformation measured by Extensometer A at the moment when the HF approached the surface of the sample, was equal to 68 μm , whereas at the same moment, Extensometer B recorded only 31 μm on the opposite side of the sample. Thus, both the AE and deformation measurements confirm asymmetry of HF propagation in the sample GM4-101.

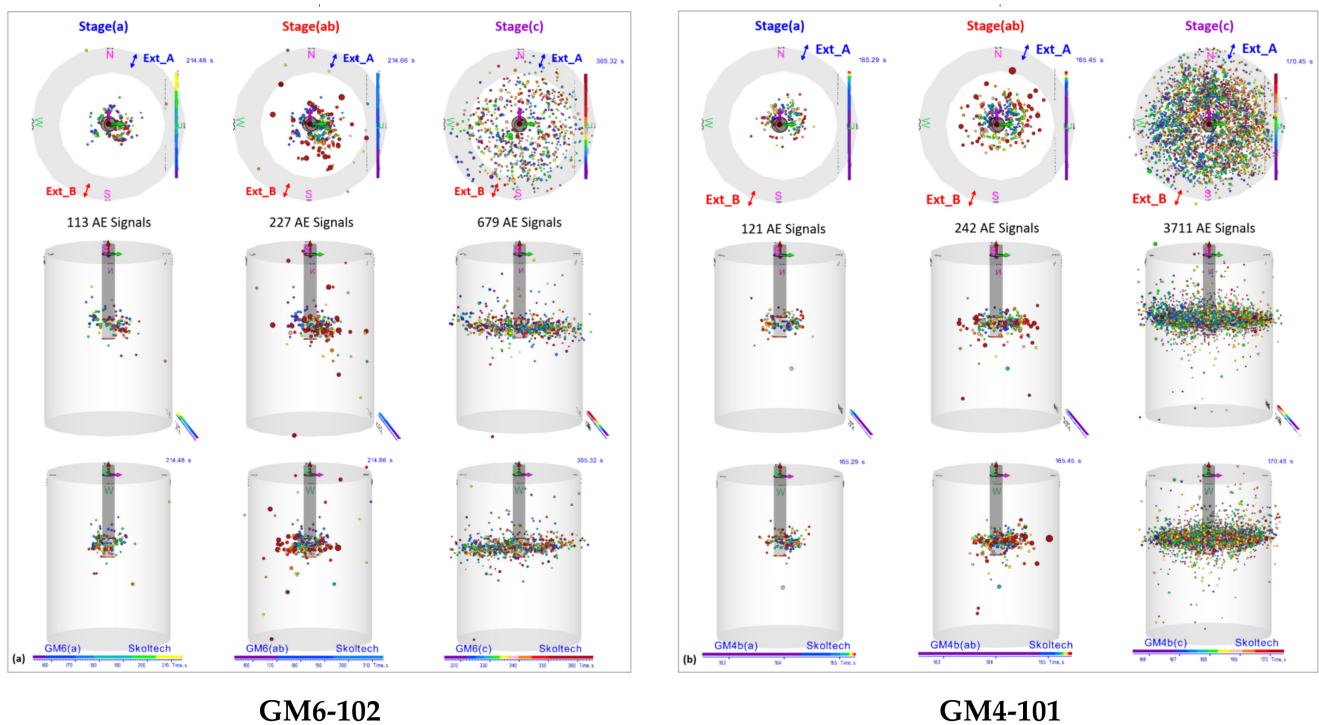


Figure 12. Three orthogonal projections of AE signal positions within the GM6-102 (a) and GM4-101 (b) samples, hydraulically fractured by low-viscosity OG injection.

The left column of the plots, labeled stage (c) (Figure 12), shows the AE activity during the final stage of the test associated with HF expansion across the entire cross-section of the sample, followed by the closure of HF. The loading algorithm was designed in such a way that, after reaching a significant HF opening, the fluid was pumped out of the wellbore and the loading piston quickly returned the displacement to its initial position, corresponding to the value of an unbroken sample, ensuring closure of the HF. The AE signals recorded during stage (c) can be radiated by squeezing rough HF surfaces, which was directly confirmed by AE Moment Tensor Inversion [27]. The observed difference in

the number of AE events may be related to the difference in elastic wave attenuation in dry and saturated samples [40]. Note that the injection of high-viscosity SO in the GM5-101 test resulted in a significantly higher number of AE events than the injection of lower viscosity OG in the GM6-102 and GM4-101 samples, as well as in a larger deformation of the sample and a larger volume injected into the HF (Figures 9 and 11, pink curves). It can be explained by the creation of HF with a larger aperture during the injection of higher viscosity fluid, which is consistent with [39]. In all performed tests, the positions of the located AE events exactly repeat the shape of the obtained fractures (Figure 13).

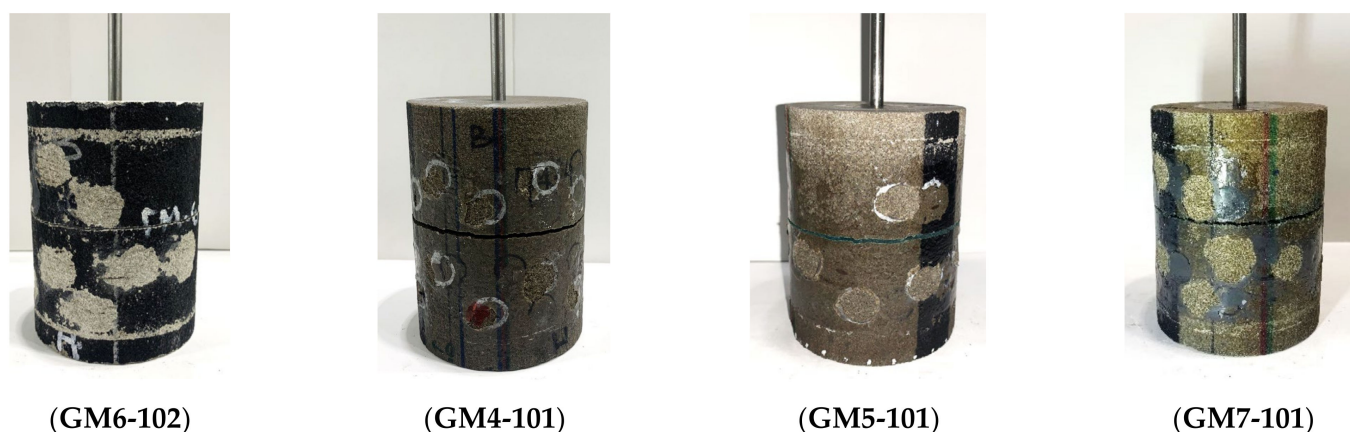


Figure 13. The specimens GM6-101, GM4-101, GM5-101, and GM7-101 after the experiment.

As shown earlier in Section 3.1, the mineral-oil-saturated sandstone specimen was characterized by lower values of Young's modulus, compressive strength, and cohesion compared to the dry sample of the same sandstone. In hydraulic fracturing experiments, we found that the saturated sample (GM4-101) had a lower BP value and a wider fracture opening compared to the corresponding parameters for the dry sample (GM6-102). However, the fracture propagation speed is higher in the dry sample (GM6-102).

3.3. Hydraulic Fracture Propagation in Original (Unheated) and Thermally Treated (TT) Granite

To supplement the results obtained for the sandstone specimens, three granite samples were prepared and tested with the OG injection (one untreated and two thermally treated samples), and, in addition, one untreated granite sample was tested with the SO injection (with a viscosity of 1000 cP). In contrast to the Newtonian SO constant viscosity, the non-Newtonian OG viscosity significantly decreased from 1220 cP at 100 rpm to 310.81 cP at 300 rpm. Hydraulic fracturing experiments were conducted on the four granite specimens at σ_1 of 22 MPa and σ_3 of 8 MPa. The horizontal fracture orientation was induced and controlled by the sample loading scheme; the induced fracture was oriented in the σ_1 plane, perpendicular to the σ_3 plane, in all tests. Fracturing fluids were injected at a constant rate of 5 mL/min. The main experimental conditions are described in Table 6.

Table 6. Relevant information about the hydraulic fracturing experiments in granite specimens.

Sample Id	σ_1	σ_3	Fracturing Fluid	Injection Flow Rate	Thermal Treatment	Saturation
-	MPa	MPa	-	mL/min	-	-
TG-701	22	8	SO 1000 cP	5	unheated	Dry
TG-717	22	8	OG	5	unheated	Dry
TG-714h	22	8	OG	5	heated	Dry
TG-715h	22	8	OG	5	heated	saturated

At first, let us look at the parameters of HF recorded in the original (untreated) granite samples fractured by the OG injection (TG-717, Figure 14, left column) and by the SO injection (TG-701, Figure 14, right column). Similarly to the sandstone tests presented above, the moment when the HF approached the sample surface was also registered very close to the moment when the highest AE amplitude was recorded (Figure 14, vertical blue dash lines). In case of the OG injection (left column), Figure 14a shows that about 1.1 s before this moment, marked by the vertical blue dashed line, an acceleration of AE activity was recorded (vertical violet dashed line) and about 0.6 s later, an onset of axial displacement was recorded (Figure 14b, green arrow), indicating that the HF has begun to open. Note that the onset of fluid infiltration into the HF was observed about 0.3 s later than the onset of displacement, or just 0.2 s before the HF reached the cylindrical surface of the rock (Figure 14c, light blue arrow). We interpret these experimental observations by assuming that propagation of the dry FPZ took place during this 0.3-s interval between the green and blue arrows. We assume that the OG could not instantly fill all the very thin microcracks, especially if not all of them were interconnected. It means that probably during the initial stage of the OG injection, there was a lag between the front of the FPZ and the fluid front, in correspondence with the results of studies [39,41] where the appearance of a delay during the injection of viscous fluid was directly confirmed by the results of ultrasonic transmission measurements.

A very similar combination of recorded parameters was observed in case of SO injection (with a viscosity of 1000 cP) into TG-701 granite; however, the absolute values of almost all the parameters were different, as the comparison of the left (fluid OG) and right (fluid SO) columns of Figure 14 shows. The injection of the fluid into the TG-701 sample caused the onset of AE activity much earlier than the moment when the HF approached the rock surface, and upon approaching the surface it showed a significantly larger number of AE signals (Figure 14i), a larger deformation of the sample (Figure 14j), a larger volume of fluid injected into the fracture (Figure 14k), and a significantly lower speed of the HF propagation (Figure 14p). We attribute the difference in all parameters, observed by several independent recording systems, to the influence of the viscosity of the injected fluid, in accordance with the results of earlier studies [25,39,41].

Similarly to the tests described above, the fracturing process of the TG-717 and TG-701 samples was also divided into three stages: stage (a) lasted until half of the number of AE signals localized before the HF approached the surface of the rock was recorded (Figure 14, light blue rectangle). Stage (b) lasted until the HF approached the cylindrical surface of the rock (Figure 14, rose rectangle), and stage (c) represents the HF closure stage (Figure 14, yellow rectangle).

Figure 15 shows three orthogonal projections of the spatial distributions of localized AE signals corresponding to three stages of HF propagation. During the initial stage (a) (left column of plots), as well as during the HF propagation up to the sample boundary (stage (ab), middle column of plots), a predominant south-east direction of HF propagation can be observed in sample TG-717 (left) and north-east in TG-701 (right). In the case of the TG7-17 sample, this direction of HF propagation is almost symmetrical in relation to the installation places of extensometers Ext_A and Ext_B (Figure 15a, upper row of plots), so the AE results correlate with insufficient difference in the recordings of two extensometers (Figure 14b left, blue and red curves). In the case of the TG-701 sample, the initial propagation of the HF was directed toward the Ext_A extensometer location marked with a blue double-headed arrow, with limited propagation towards the Ext_B extensometer (Figure 15b, upper row of plots), so there was a significant difference between the values recorded by both extensometers (Figure 14j right, blue and red curves). Thus, for both tests, there was a close correspondence between the independent techniques (AE and deformation measurements). In the case of the TG-701 test, both methods indicated an asymmetry of the created HF.

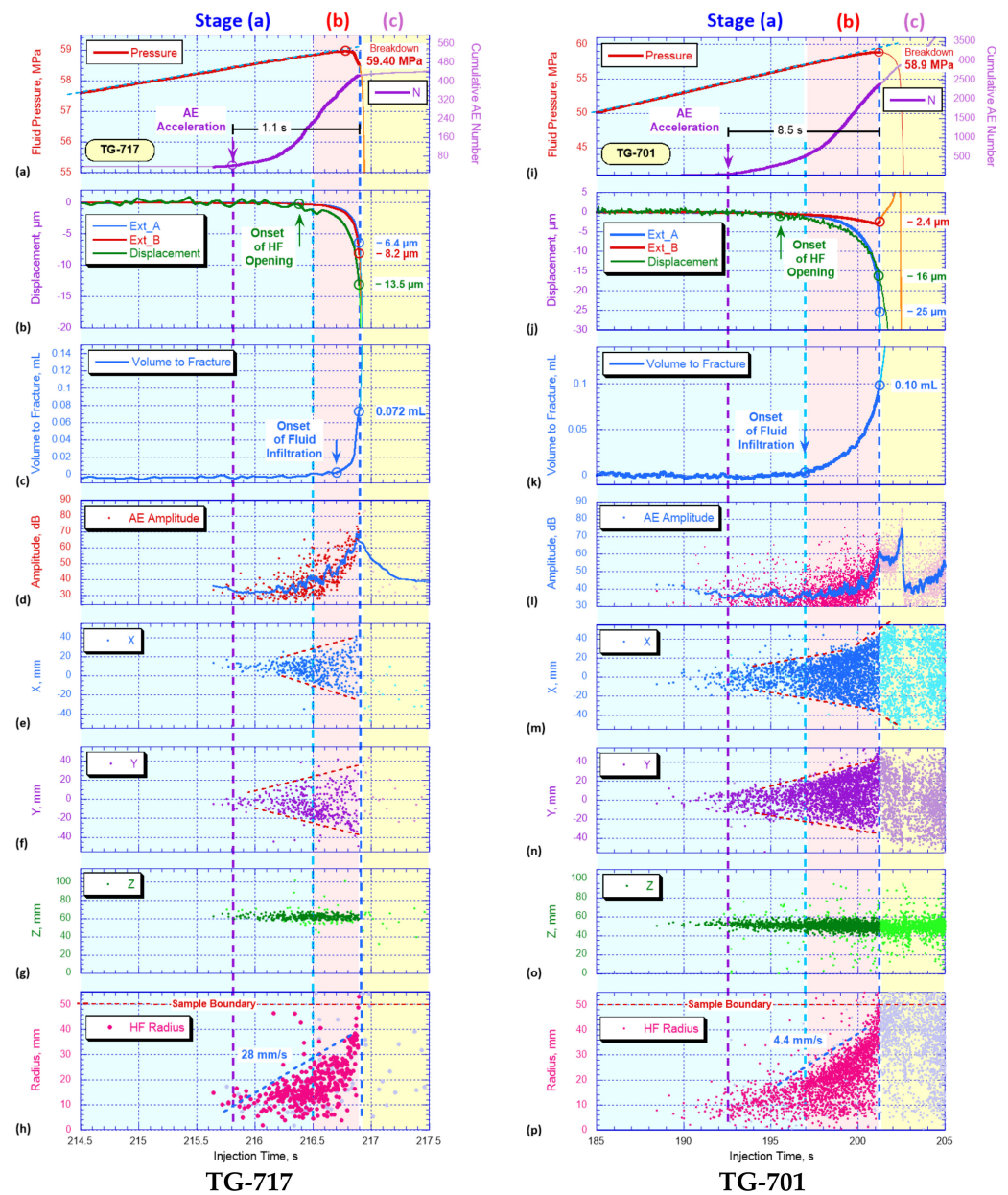


Figure 14. (a,i) fluid pressure (red) and total number of located AE signals (purple); (b,j) axial deformations measured by the left (Ext_B, red) and right (Ext_A, blue) extensometers and a curve demonstrating the piston position (green); (c,k) the volume of fluid injected into the hydraulic fracture; (d,l) amplitudes of AE signals; (e,f,m,n) horizontal coordinates of the located AE signals in the X and Y directions, respectively; (g,o) vertical coordinates of the localized AE signals; (h,p) distribution of the distances between the located AE signals and the axis of the sample. All parameters for TG-717 and TG-701 samples are plotted versus the time of sample testing.

Let us turn to the study of the HF properties in thermally treated granites. Samples TG-714h and TG-715h were treated in the abovementioned heating procedure, up to 800 °C, in order to simulate highly fractured materials. The same viscous OG was injected in both tests, but sample TG-714h was tested dry and sample TG-715h was fully saturated with mineral oil prior to hydraulic fracturing. A comparison of the parameters recorded during hydraulic fracturing of dry TG-714h and saturated TG-715h samples is shown in Figure 16. It was found that the saturated specimen, TG-715h, demonstrated a 13% lower BP (Figure 16i, red curves) and an about 58% smaller HF aperture (Figure 16j). These results correspond well to the results described above for the pair of dry and saturated sandstones.

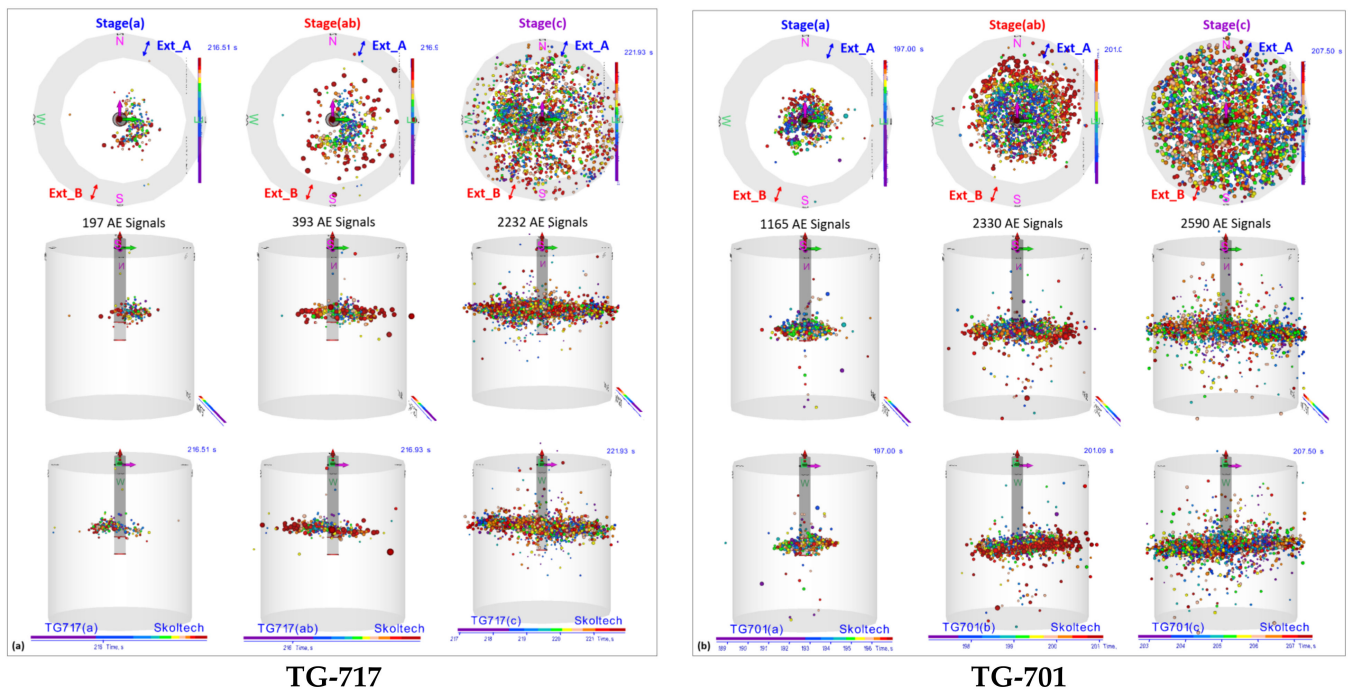


Figure 15. Three orthogonal projections of the AE signal positions in the space of the TG-717 sample hydraulically fractured by OG injection (a) and the TG701 sample fractured by SO injection (b).

It should be noted that a significant leak-off effect was detected during the OG injection into both thermally treated samples. The slopes of the red dashed lines in Figure 16c,k indicate that the highest infiltration rate was about 2.8 mL/min for the dry sample TG-714h (Figure 16c), and about 1.8 mL/min for the saturated sample TG-715h (Figure 16k). Despite the significant leak-off rate difference, the volume of fluid injected into the fracture was almost the same: 0.24 mL (dry sample) and 0.28 mL (saturated sample). In addition, we found out that the fracture propagation rate in the dry sample (Figure 16h) was almost two times slower than in the saturated sample (Figure 16p). The obvious explanation is the influence of the fluid infiltration rate on the dynamics of hydraulic fracture propagation. The injection rate was equal to 5 mL/min in both samples. Taking into account that the fluid infiltration rates in the dry and saturated samples were 2.8 and 1.8 mL/min, respectively (Figure 16c); it can be assumed that the fluid flows towards the tip of the hydraulic fracture in the dry and saturated samples were 2.2 and 3.2 mL/min, respectively. Most likely, this difference is the cause of the different registered rates of fracture propagation.

In addition, we found several differences in the spatial distribution of AE events in the dry and saturated samples, as shown in Figure 17. In the saturated sample (TG-715h) the HF propagated within a small sector, mainly between the south-east and north-east directions (Figure 17b). In the dry sample (Figure 17a), AE events were distributed in a wider segment, mostly between the south-east and north directions. Furthermore, 3724 AE events were recorded in the saturated sample and only 357 signals were recorded in the dry sample, which corresponds to the number of AE events registered earlier in a pair of the dry and saturated sandstone specimens. For all studied granite samples, the AE event distributions coincide with the shapes of the observed fractures (Figure 18).

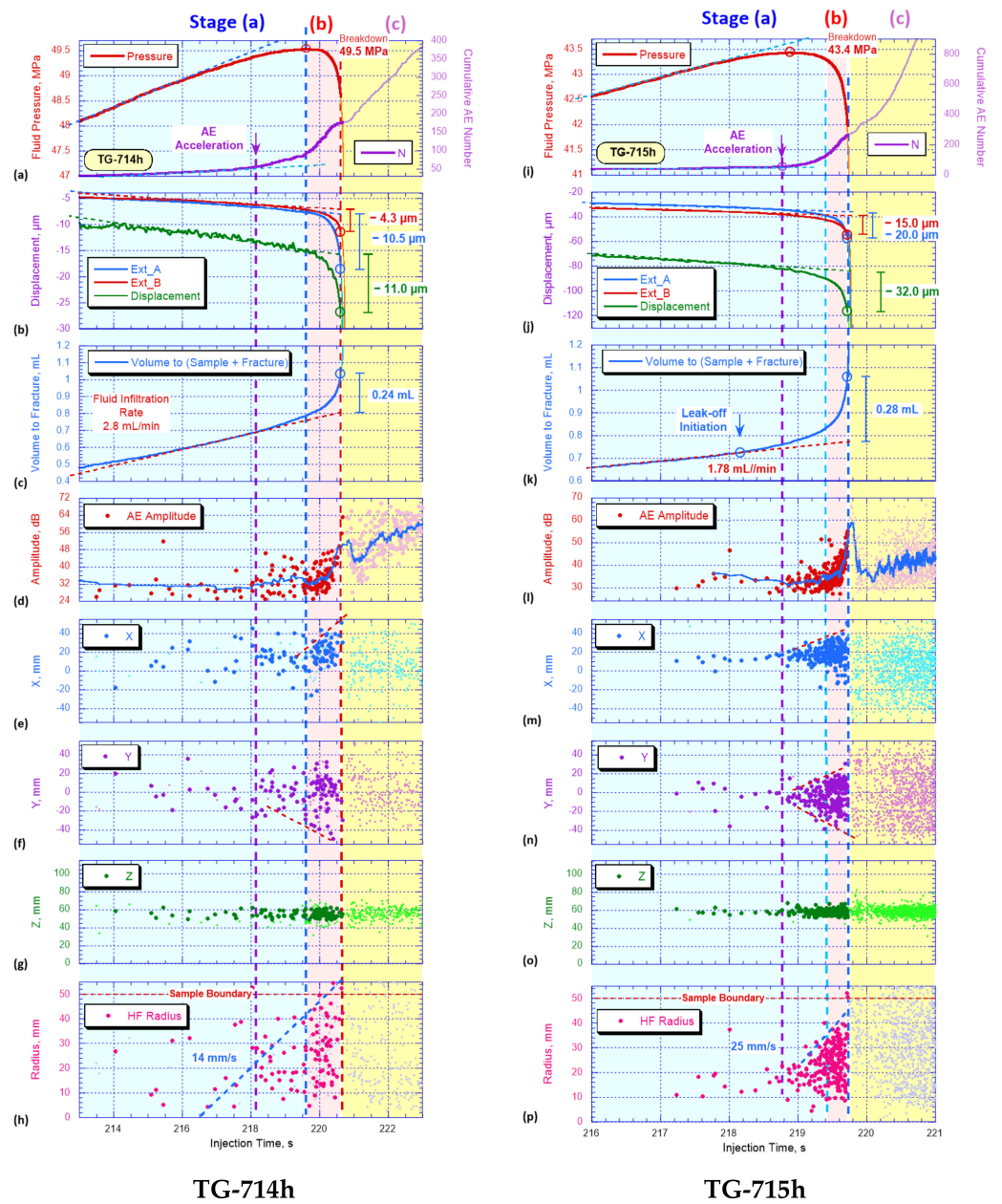


Figure 16. (a,i) fluid pressure (red) and total number of AE signals located (purple); (b,j) axial deformations measured by the left (Ext_B, red) and right (Ext_A, blue) extensometers and a curve demonstrating piston position (green); (c,k) the volume of fluid injected into the hydraulic fracture; (d,l) amplitudes of AE signals; (e,f,m,n) horizontal coordinates of the located AE signals in the X and Y directions, respectively; vertical coordinates of the located AE signals; (g,o) vertical coordinates of the localized AE signals; (h,p) distribution of the distances between the located AE signals and the axis of the sample. All parameters are plotted versus the time of sample testing.

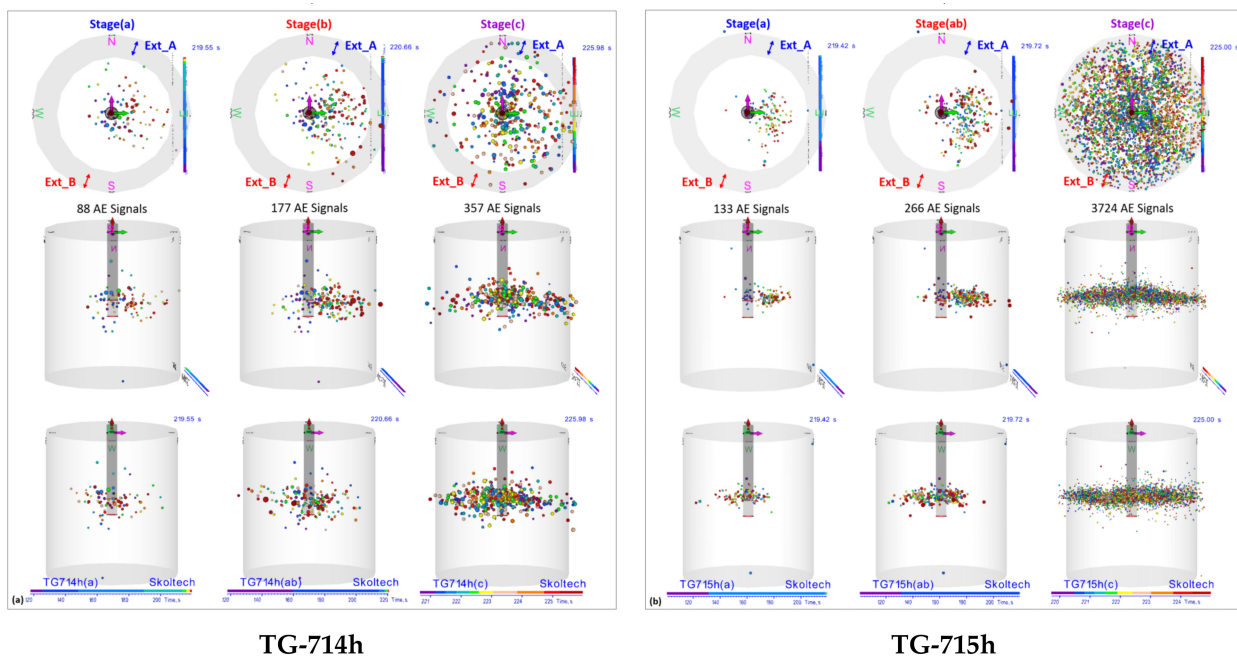


Figure 17. Three orthogonal projections of AE signals positions within the TG-714h (a) and TG-715h (b) samples, hydraulically fractured by low-viscosity OG injection.

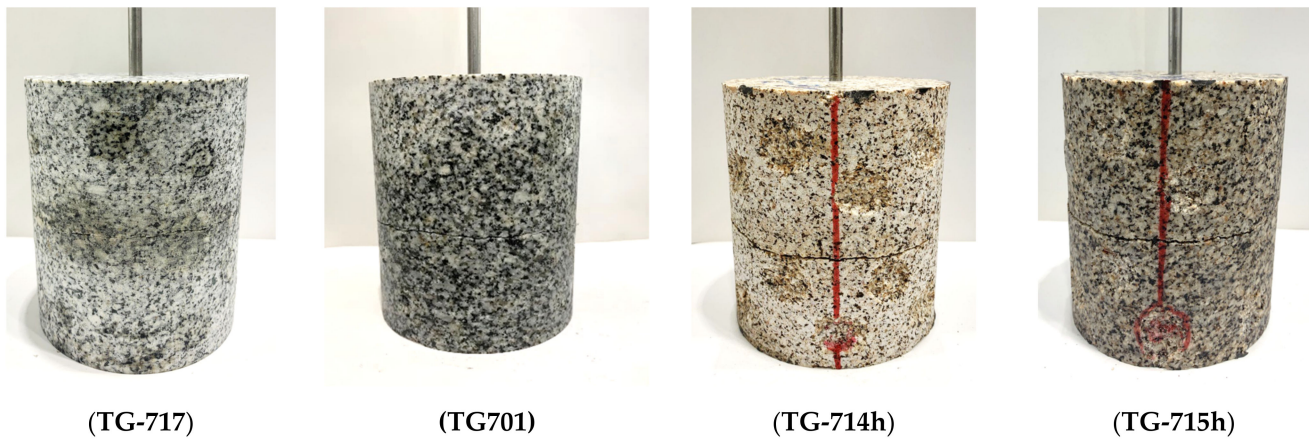


Figure 18. Photos of the TG-717, TG-701, TG-714h and TG-715h specimens after the test.

4. Discussion

In our research, the fracturing process was investigated in the dry and mineral-oil-saturated rocks, such as sandstone, unheated granite and thermally treated (TT) granite. Before starting the hydraulic fracturing experiments, we measured the effective porosity and permeability and carried out a set of triaxial compressive tests to determine the mechanical and acoustic properties of studied rocks. These characteristics of the dry and mineral-oil-saturated sandstone specimens are listed in Table 4, and the same characteristics for the unheated granite and dry and mineral-oil-saturated TT granites are represented in Table 2. The influence of mineral oil saturation on the strength and elastic properties of investigated sandstone and TT granite is shown in Figure 19. It was observed that the mineral oil saturation (Sandstone GM2) caused a small reduction in the values of the sandstone properties. The values of comprehensive strength decreased from 175.06 MPa to 166.67 MPa; the values of Young’s modulus decreased from 14.36 GPa to 14.13 GPa. However, the most significant reduction in values of the granite properties was caused by high-temperature heating (the value of comprehensive strength decreased from 447.62 MPa to 389.13 MPa and the value of Young’s modulus decreased from 62.55 GPa to 21.28 GPa),

while mineral oil saturation demonstrated much less significant influence on the TT granite properties (the value of comprehensive strength decreased from 389.13 MPa to 333.20 MPa and the value of Young's modulus decreased from 21.28 GPa to 18.25 GPa).

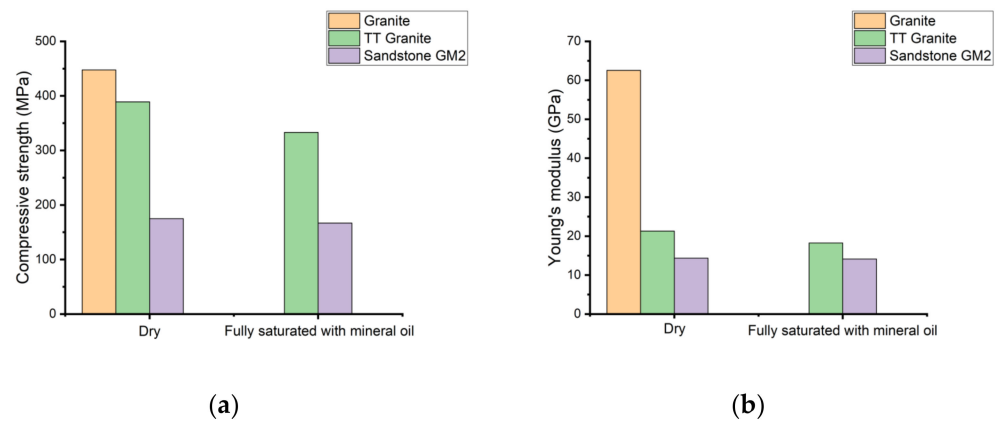


Figure 19. (a) Compressive strength versus saturation; (b) Young's modulus versus saturation.

The comparison of the experimental results of the hydraulic fracture initiation and propagation in the dry (GM6-102) and mineral-oil-saturated (GM4-101) sandstone specimens demonstrated that parameters such as fracture aperture and fracturing agent volume were larger, and breakdown pressure was lower in the saturated specimen. In addition, the comparison of those fracture parameters, obtained in the tests with the dry (TG-714) and mineral-oil-saturated (TG-715) TT granite samples, showed similar behavior (Figure 20a). These results are consistent with the previous research [42] and confirm that rocks with a reduced elastic modulus, caused by saturation and high-temperature heating, can experience large deformations and require less stress to cause them. Therefore, it is typical for the saturated and TT specimens to have a wider width of fracture induced by a lower fluid pressure (Figure 20b).

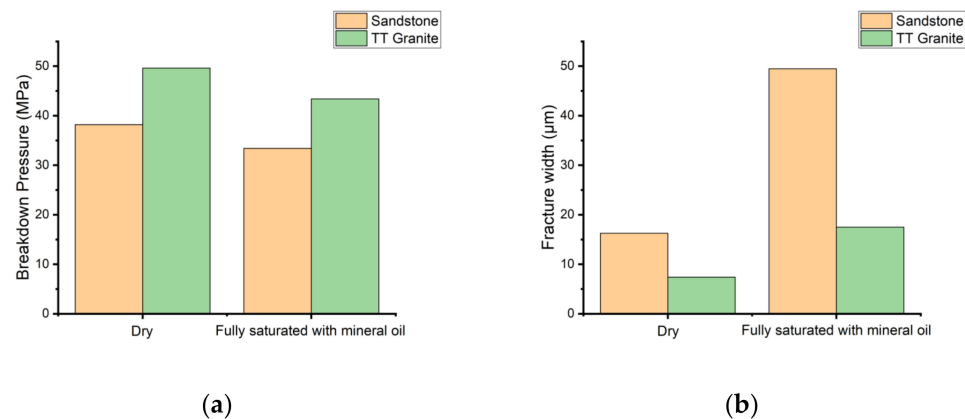


Figure 20. (a) Breakdown Pressure versus mineral-oil saturation; (b) fracture width versus mineral-oil saturation.

The analysis of obtained fracturing results revealed a strong correlation between the mechanical properties of the rock and the parameters of fracture generated in the rock. The unheated granite is characterized by the highest Young's modulus and compressive strength values, and the highest value of BP was predictably observed, similar to [43]. Meanwhile, BP and fracture aperture, as well as their mechanical parameters, decreased in both mineral-oil-saturated sandstone and TT samples, shown in Figures 21 and 22. The obtained correlations align well with [42,44–46]. The described findings could be associated with the preliminary exposure of the rock matrix to saturation and thermal treatment.

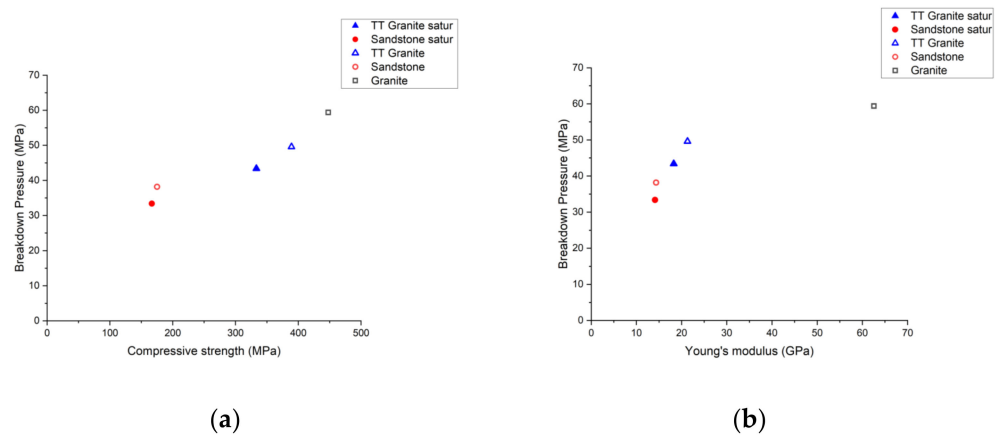


Figure 21. (a) Breakdown pressure versus compressive strength; (b) breakdown pressure versus cohesion.

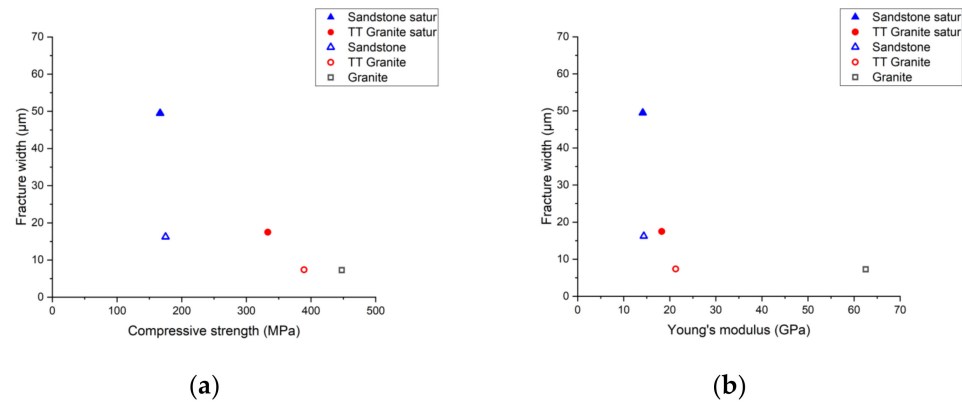


Figure 22. (a) Breakdown pressure versus indirect tensile strength; (b) fracture aperture versus Young's modulus.

The Mohr–Coulomb circles were plotted and failure criteria were calculated for two pairs of «twin» sandstone samples. Figure 23 demonstrates a less significant reduction in cohesion from 18.8 MPa to 17.6 MPa for the dry GM2-001 and mineral-oil-saturated GM2-002 specimens, respectively. We may suppose that partial losses in cohesion, elasticity, and strength have been caused by an absorption effect of clay contained in the sandstone matrix. The presence of clay minerals (illite, kaolinite, and chlorite) in the sandstone mineral composition was confirmed by the XRD analysis presented in Figure 5.

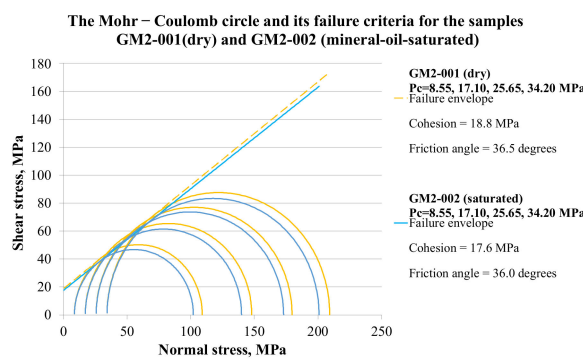


Figure 23. The Mohr–Coulomb circles for the dry GM2-001 and mineral-oil-saturated GM2-002 «twin» samples.

In addition, the Mohr–Coulomb circles were plotted and failure criteria were calculated for the unheated (TG-004), dry TT (TG-020), and mineral-oil-saturated TT (TG-029) granite

samples. The most significant decrease in cohesion values (from 31.4 MPa to 15.8 MPa) was caused by the high-temperature heat treatment, while the decrease in cohesion values (from 15.8 MPa to 14.1 MPa), caused by the mineral oil saturation procedure, was much less significant. The main reason for the losses in elastic and strength properties was a dense fracture network, which was an outcome of the high-temperature treatment. The article [47] confirmed that the thermally induced fracture network is a major source of weakening of the TT granite mechanical properties (Figure 24).

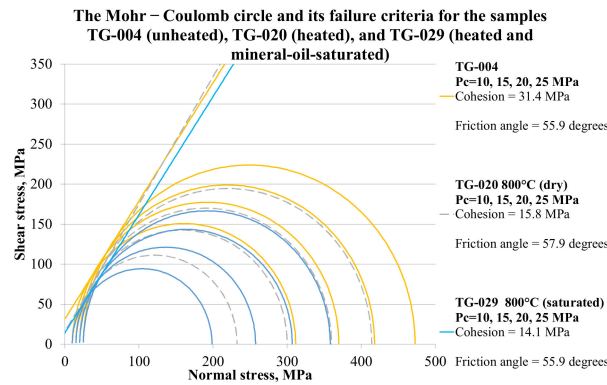


Figure 24. The Mohr–Coulomb circles for the unheated (TG-004), TT (TG-020), and TT and mineral-oil-saturated (TG-029) granite samples.

The hydraulic fracturing experiments were monitored by a combination of independent systems, such as AE monitoring and pressure, volume and deformation sensors. Such a comprehensive monitoring installation is inaccessible in a reservoir; however, in a laboratory, as it was revealed, it is possible to measure the changes in fracture parameters during the growth of hydraulic fracture. The obtained features of fracture development should be investigated in the laboratory conditions on the target core samples, and the experimental findings can be used to verify the hydraulic fracture model. The results of hydraulic fracturing laboratory tests on the sandstone, unheated granite, and TT granite samples are presented in Table 7.

Table 7. Generalized results of hydraulic fracturing studies.

Sample Id	GM4-101	GM6-102	GM5-101	GM7-101	TG-701	TG-717	TG-714h	TG-715h
Fracturing fluid	Saturated OG	Dry OG	Saturated SO	Saturated SO	Dry SO	Dry OG	Dry OG	Saturated OG
Fluid viscosity μ at 100/sshear rate, cP	1220	1220	10,000	100,000	1000	1220	1220	1220
σ_1 , MPa					22			
σ_3 , MPa					8			
Breakdown pressure P_b , MPa	33.4	38.2	49.8	53.1	58.9	59.40	49.6	43.4
Fluid volume, having entered the fracture, mL	0.34	0.16	0.4	0.31	0.098	0.28	0.24	0.28
Fracture width, μm	68/31	13.5/19.0	85.6/80.6	75.4/78.2	25/2.4	6.4/8.2	10.5/4.3	20.0/15.0
Fracture propagation velocity, mm/sec	40	70	15	3	4.4	28	14	24

As for AE monitoring, it provided valuable information about the fracture dynamics and the stimulated region during a fluid injection. It was demonstrated that the injection of the high-viscosity fracturing agent, such as SO (a viscosity of 10,000 cP or 100,000 cP), induced a radial and symmetrical fracture in the GM5-101 and GM7-101 samples. The top view of the coordinates of the located AE events (Figure 25, upper illustration) displayed a precise radial shape of the FPZ propagation during the experiment. An injection of lower viscosity OG induced a less symmetrical spread of the radial fracture front in the sandstone samples (Figure 25, middle illustration) and narrow-sector fracture propagation in the granite samples (Figure 25, lower illustration). These findings are consistent with the

results of the previous study [25], conducted on another granite with a low-viscosity fluid injection. A comparison of normalized densities of localized AE events in the GM5-101, GM4-101, and TG-715h samples at the moment when HF approached the sample boundary is shown in Figure 26. The analysis of the presented AE densities indicated that only in the case of high viscosity SO injection into the sandstone sample (GM5-101) the created HF had a symmetrical radial shape (Figure 26a). Hence, both Figures 25 and 26 demonstrate that the observed fracture shape may significantly differ from radial, which is widely used in penny-shaped models, because of the prevailing influence of the fracturing fluid viscosity and the rock matrix.

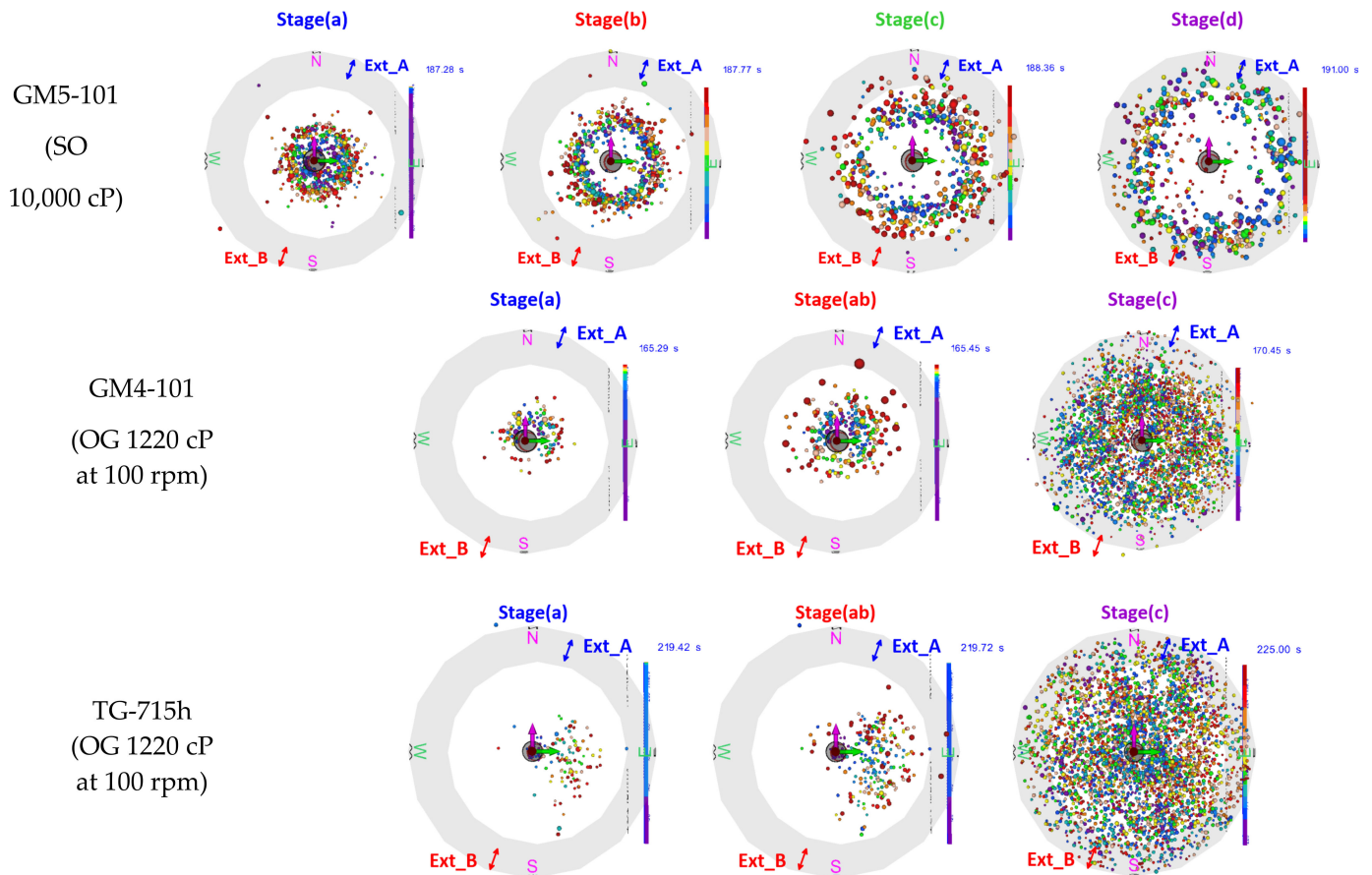


Figure 25. Top view of the located AE events in the GM5-101, GM4-101, and TG-715h samples.

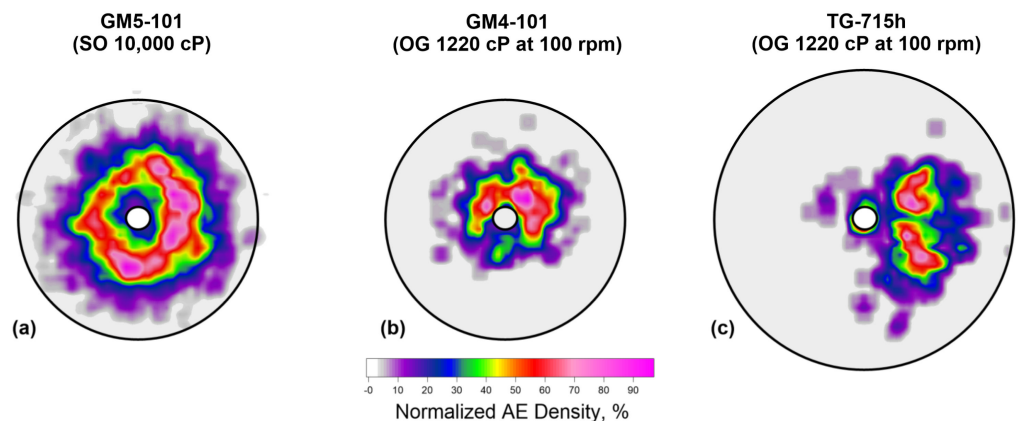


Figure 26. Top view of normalized density the located AE events in the GM5-101 (a), GM4-101 (b), and TG-715h (c) samples.

Additionally, the activity of AE in the mineral-oil-saturated samples was higher than in the dry ones. For example, 3711 events were located in the mineral-oil-saturated sample (GM4-101), whereas only 379 events were observed in the dry GM6-102 sample. Similar proportions of AE events were also observed in the mineral-oil-saturated TG-715h (3724 AE events) and the dry TG-714h (357) TT granites. The AE amplitude, as well as a cumulative number of located AE events, was expectedly higher in saturated samples. The observed difference may be related to the lower attenuation of elastic waves in fully saturated samples.

The results of P-wave velocity measurements in all tested samples, during the increase of confining pressure, are shown in Figure 27. P-wave velocities in the dry samples (TG714h, GM6-102) are the lowest, P-wave velocities in the mineral-oil-saturated samples (TG715h, GM5-101) are in the middle range of values, and the highest P-wave velocity was recorded in the unheated granite sample (TG-717) (Figure 27). This means that the correct correlation of laboratory results and well log data requires the investigation of saturated samples. Note that the values of P-wave velocities measured in saturated sandstone (GM5-101) and in saturated thermally treated granite (TG-715h) samples differ by less than 10%, so we believe that thermally treated granite can be used to model the hydraulic fracture in porous rocks.

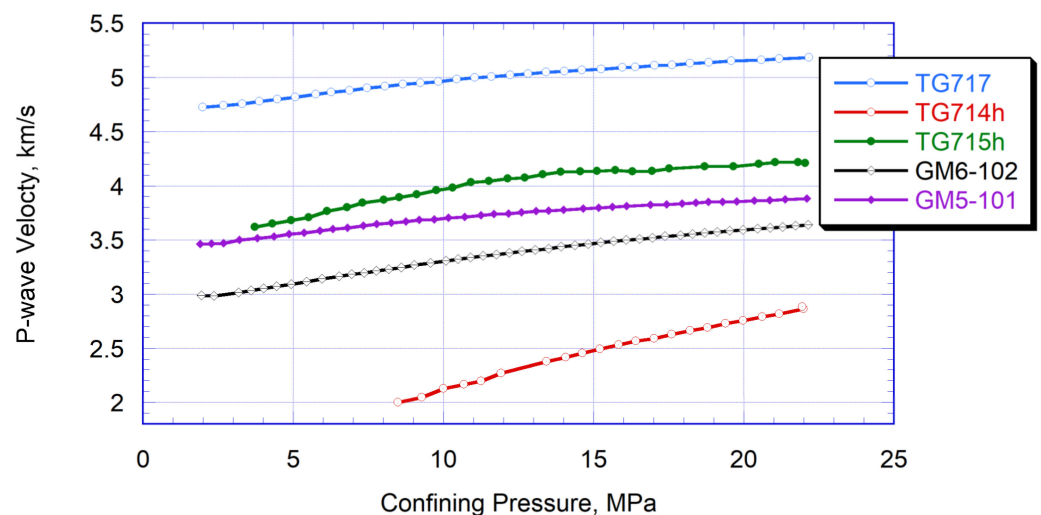


Figure 27. The traces of P-wave velocities for the samples versus confining pressure.

Additionally, the comparison of the fracture parameters measured during the injections of fluids with different viscosities was also analyzed. It was shown (Figure 28) that an injection of high-viscosity SOs (10,000 cP and 100,000 cP) caused a higher value of BP and a wider fracture opening. Additionally, injection of less viscous OG with variable viscosity induced the fracture with a lower BP and a narrower fracture opening. These observations correlate well with the results of previous research [25,38]. Comparing the non-Newtonian OG and Newtonian SO with the similar viscosities at 100 rpm, OG-driven fracturing demonstrated a slightly higher pressure value and a smaller fracture opening, which can be associated with a significant decrease in viscosity at 300 rpm. The observed correlation is applicable to the mineral-oil-saturated sandstone and to unheated granite.

The last part of the study describes fracture initiation and propagation in the highly fractured rock matrix. Studies [48,49] have revealed that the propagation of hydraulic fractures in a naturally fractured environment is quite complex. The influence of natural fractures and in situ local stresses on the initiation, propagation, and orientation of hydraulic fractures in the reservoir during the fracturing process remains an important issue. To assess the stimulated reservoir volume (SRV) and the efficiency of the field HF operations, it is necessary to understand how pre-existing discontinuities affect the induced hydraulic fracture.

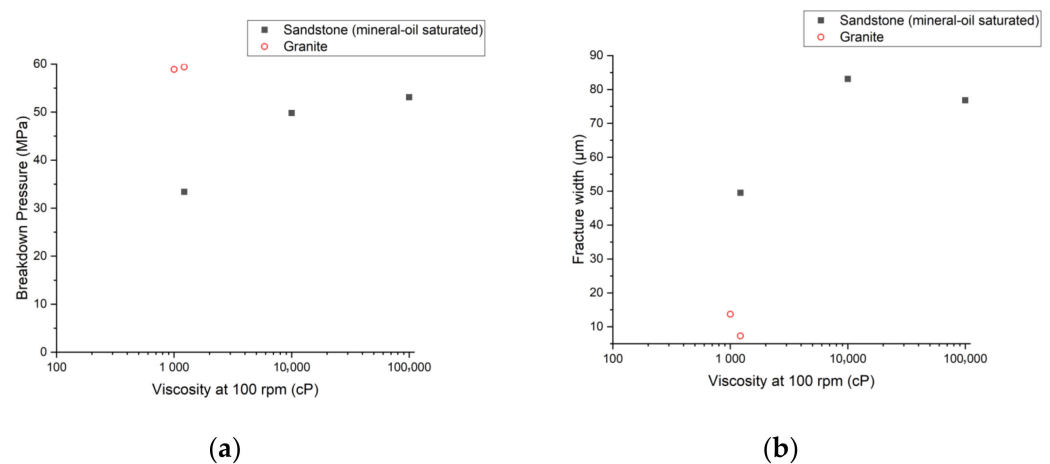


Figure 28. (a) Breakdown pressure versus fracturing fluid viscosity; (b) fracture aperture versus fracturing fluid viscosity.

The thermally treated (TT) (TG-714 and TG-715) granite specimens were prepared and tested under the same conditions and the OG-fluid was injected in all three experiments. The samples (TG-714h and TG-715h) were heated up to 800 °C with the purpose of simulating fractured materials. The same viscous OG was injected, but the sample TG-714 was tested dry, and sample TG-715h was fully saturated with mineral oil before the injection. Figure 29 shows a comparison of the mechanical data recorded during the injection of fluid into the dry (left) and saturated (right) TT samples. Red curves in the upper row of plots in Figure 29 show the pressure in the wellbore increasing linearly at the initial part of the fluid injection and deviating from the linear trend at a later stage. The bottom row of plots in Figure 29 shows the volume of fluid injected into the hydraulic fracture, calculated as described above by subtracting the linear trend of injected volume increase. Note that there was no increase in AE activity associated with the onset of injected volume increase, so it could not be related to the initiation of hydraulic fracture. However, approximately at the same time, marked by the light blue vertical dash line, we observed the onset of independently measured deformations in both samples (middle row of plots in Figure 29); therefore, we believe that the increase in the injected volume had to occur due to the fluid leak-off inside highly fractured samples. The analysis of these blue curves in the bottom row of the plots in Figure 29 shows that the leak-off began at fluid pressures, 26.7 and 16.5 MPa, and that the fluid infiltration rates at the moment of hydraulic fracture initiation were 2.8 mL/min and 1.8 mL/min for dry and saturated samples, respectively. Since the fluid injection rate was equal to 5 mL/min, or higher than the fluid leak-off rates, both TT samples were successfully fractured, but the presence of infiltration affected the fluid flow towards the tip of the fracture, that may have resulted in different fracture dynamics. Therefore, our experimental studies confirmed that the leak-off should be taken into account during hydraulic fracturing of reservoirs with a high density of natural cracks.

Authors pay much attention to the fracture surface investigation due to the expected problems with successful proppant transport and distribution along rough HF surfaces. Analysis of the fracture surface roughness showed that the sandstone (GM6-102) is characterized by the almost flat fracture surface, in contrast to TT granite, which has a much rougher HF surface (Figure 30). That is why the structure of the rocks should be taken into account in the field HF simulations.

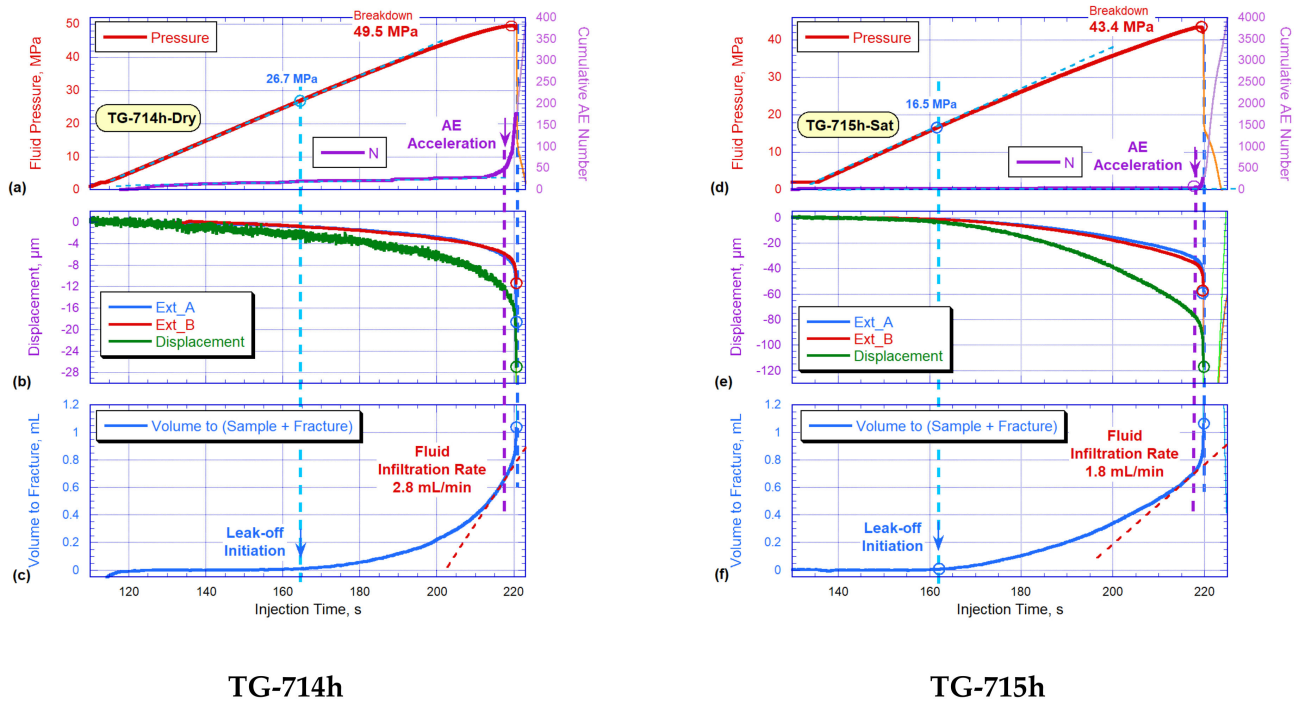


Figure 29. Samples TG-714h dry (left) and TG-715h saturated (right): (a,d) fluid pressure (red) and a total number of AE signals located (purple); (b,e) axial deformation measured by the left (Ext_B, red) and right (Ext_A, blue) extensometers and a curve demonstrating the loading piston position (green); (c,f) the volume of fluid injected into the hydraulic fracture. All parameters are plotted versus the time of sample testing.

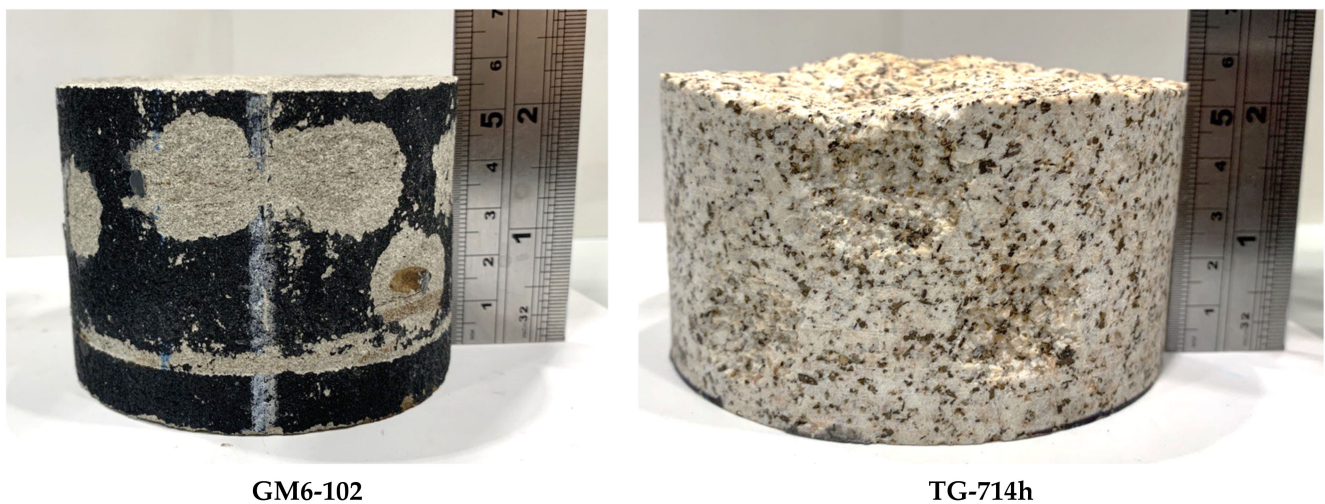


Figure 30. Samples GM6-102 (left) and TG-714h (right).

The comparison of the grain sizes of sandstone and TT granite is provided in Figure 31. The size of sandstone grain is up to 0.5 mm, whereas the size of TT granite grain is 3–5 mm.

Laser scanning of the created hydraulic fracturing surfaces was carried out, which allowed us to obtain 3D images of the fracture surfaces with the accuracy of 50 μm. Figure 32a shows 2D maps of fracture surface topography, plotted on the basis of laser scanning of the fractured samples. Figure 32b demonstrates the top-view of AE signals located during the initial stage of hydraulic fracturing propagation, where the fracture did not reach the cylindrical surface of the sample, and the fluid did not spread along the cylindrical surface of the sample below the impermeable jacket and did not cause a change in the stress distribution within the sample. Figure 32c demonstrates the sector of the fracture surface, which

was selected for the analysis of HF surface parameters on the base of a spatial distribution of AE events during the initial stage of the experiment (Figure 32b).

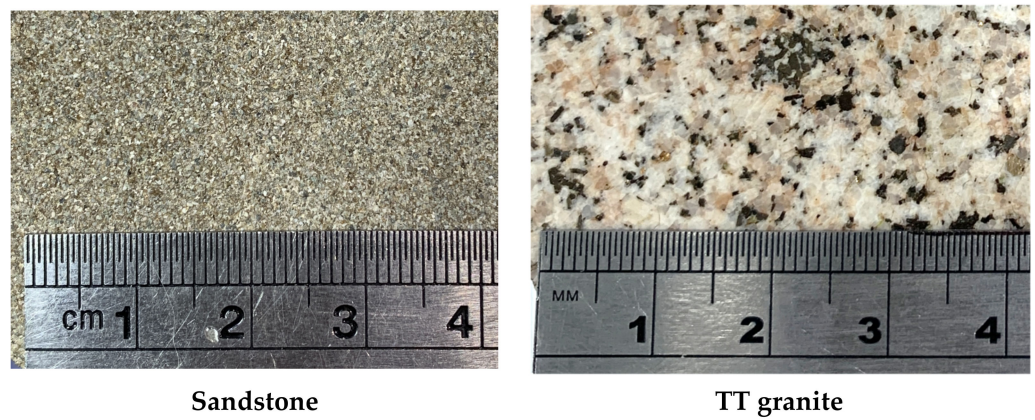


Figure 31. The appearance of the sandstone and TT granite.

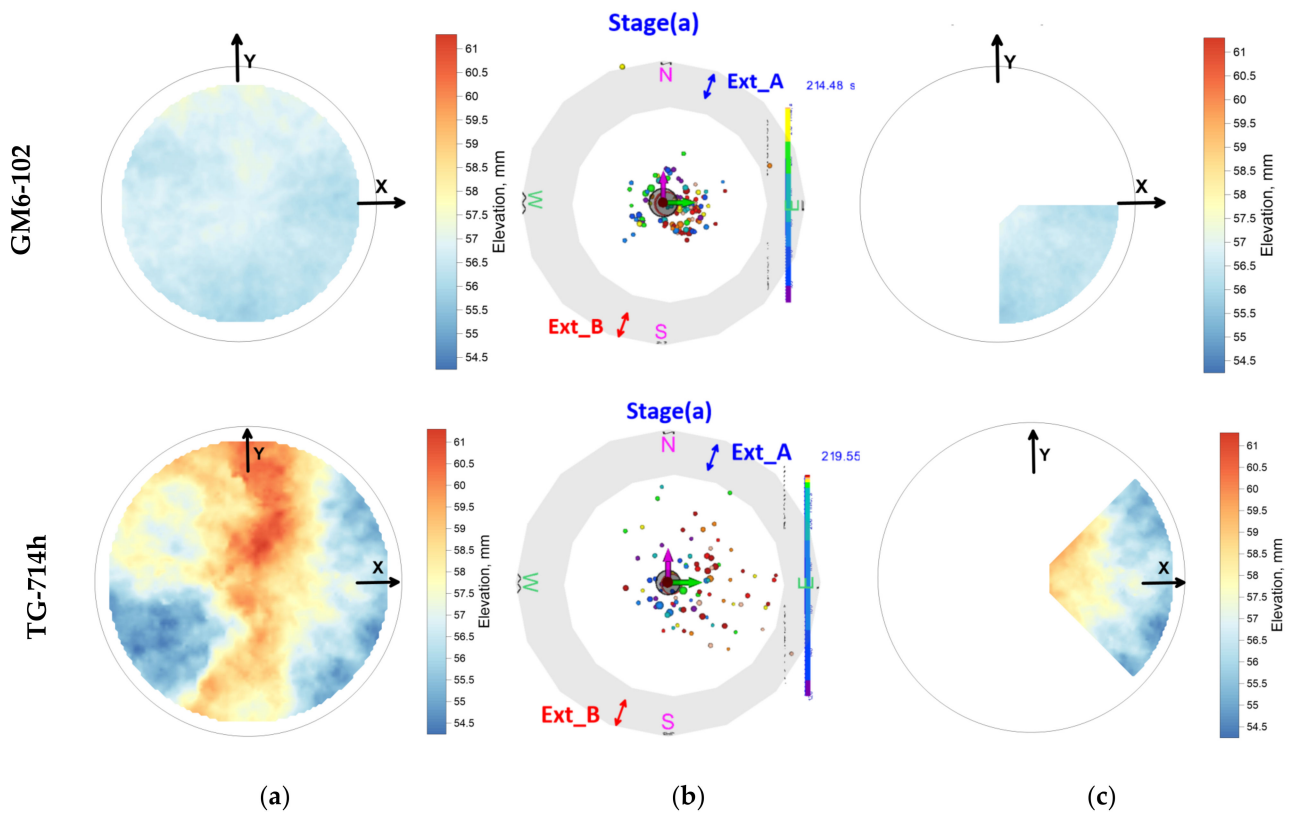


Figure 32. The top view of (a) 2D fracture surface maps of the samples; (b) localizations of AE signals recorded during the initial stage of HF propagation; and (c) sectors selected for the analysis of fracture topography.

The main statistical surface roughness parameters for the dry samples (GM6-102 and TG-714) are listed in Table 8. The peak asperity height R_p , the average roughness R_m , the root-mean-square roughness R_{rms} , and tortuosity were calculated according to formulas and detailed explanation provided in [25]. The parameter Z_{1-2} is calculated as a sum of the biggest positive perpendicular distance from the base plane and the absolute value of the largest negative perpendicular distance from the base plane. This parameter is three times larger for the TT granite sample than the one for the sandstone sample. The calculated HF surface parameters, such as roughness R_{rms} and tortuosity, show the quantitative difference between the shapes of created HF surfaces, demonstrated in the photos in Figure 30—TT

granite sample (TG-714) has larger values of R_{rms} and tortuosity than the sandstone sample (GM6-102). In our study, we have demonstrated that the rock structure and grain size have significant influence on the morphology of the fracture surface.

Table 8. Statistical surface roughness parameters of selected samples.

Sample Id	R_p , mm	R_m , mm	R_{rms} , mm	Tortuosity	Z_{1-2} , mm
GM6-102	0.62	0.15	0.19	1.01	1.08
TG-714h	1.90	0.45	0.55	1.10	3.34

5. Conclusions

Laboratory hydraulic fracturing tests were carried out on sandstone and unheated and thermally treated granite, in both saturated and unsaturated conditions. Experimental parameters such as breakdown pressure, hydraulic fracture aperture, volume of fluid injected into the hydraulic fracture, and fracture propagation velocity were measured during the tests and used to evaluate fracture behavior. The obtained results are summarized as follows:

1. The saturation state of the sandstone and TT granite samples caused a reduction in values of mechanical parameters such as Young's modulus, compressive strength, and cohesion, and an increase in the values of P- and S-wave velocities (acoustic parameters). The described changes in the values of the mechanical properties of the studied samples resulted in changes in the values of in hydraulic fracturing parameters.
2. It was revealed that the saturation state had a similar reducing influence on the breakdown pressure; however, the values of HF parameters, such as fracture aperture and volume of fracturing agent injected into the HF, are higher in the tests for both saturated sandstone and saturated TT granite.
3. It has been found that thermal treatment of granite samples led to a much more significant decrease in the values of mechanical and acoustic parameters than mineral oil saturation. High-temperature heating led to a creation of a dense network of cracks, which was confirmed by ultrasonic velocity measurements. The presence of thermally induced cracks caused the appearance of a leak-off, with its rate becoming significant at fluid pressures above 16 MPa, and this leak-off was higher in the dry TT granite than in the saturated one. The most desirable values of HF parameters (lower BP, wider aperture, lower leak-off) were obtained during the fracture propagation in the saturated TT granite sample.
4. It has also been found that the injection of a more viscous fluid caused a hydraulic fracture with a higher value of breakdown pressure and a wider fracture aperture for both dry and saturated samples.
5. Our experimental studies confirmed that the fluid leak-off should be taken into account during the hydraulic fracturing of reservoirs with a high density of natural cracks. In order to create a successful HF in the presence of natural cracks, the rate of fluid injection should be higher than the rate of fluid penetration into the permeable matrix, decreasing fluid flow towards the hydraulic fracture tip.
6. In addition, the fracture surface profiles were investigated for sandstone and TT granite specimens. It was found that rock structure affects the HF surface roughness significantly. To obtain successful proppant transport and a wide proppant distribution along the created hydraulic fracture, rock structure should be taken into account during the process of hydraulic fracturing in field conditions.
7. We found that the mineral oil saturation of the sample resulted in a 14% decrease in the BP value for both sandstone and TT granite, whereas thermally induced fractures in the granite sample caused a 20% decrease in the BP value. The results of our laboratory experiments demonstrate that the saturation state and the presence of pre-existing fractures can significantly influence HF parameters. Obtained laboratory results should be taken into account in the modeling of hydraulic fracturing in the field.

Author Contributions: Conceptualization and methodology, A.S. and S.S.; software, S.S., E.F., T.K. and A.S.; validation, S.S. and A.S.; formal analysis, investigation, A.S., S.S. and T.K.; data curation, V.S.; writing—original draft preparation, A.S.; writing—review and editing, S.S., A.S. and E.F.; visualization, S.S., A.S., E.F. and T.K.; supervision, project administration, S.S. and M.S. All authors have read and agreed to the published version of the manuscript.

Funding: This research was funded by the Ministry of Science and Higher Education of the Russian Federation under agreement No. 075-10-2022-011 within the framework of the development program for a world-class Research Center.

Data Availability Statement: The data presented in this study are available on request from the corresponding author.

Acknowledgments: The authors would like to thank Vladimir Efstadiu and Nikita Lipatov for conducting the experiments and preparation of samples. We are also very thankful to Mikhail Spasennykh for providing sandstone samples and discussing the results. Moreover, the authors are grateful to Sergey Borodin and Lyubov Magadova for providing the fracturing fluid OilGel 40/40. Additionally, the authors would like to express their gratitude to laboratory members of the Center for Petroleum Science for technical support.

Conflicts of Interest: The authors declare no conflict of interest.

Nomenclature

Symbol	Designation	Unit
$\sigma_1, \sigma_2, \sigma_3$	Maximum, medium, minimal principal stress	MPa
μ	Fluid viscosity	cP
ρ	Density of rock	g/cm ³
φ	Friction angle	°
ν	Poisson's ratio	-
C	Cohesion	MPa
E	Young's modulus	GPa
P_b	Breakdown pressure	MPa
P_c	Confining pressure	MPa
R_p	Peak asperity height	mm
R_m	Average roughness	mm
R_{rms}	Root-mean-square roughness	mm

References

- Zhou, F.; Su, H.; Liang, X.; Meng, L.; Yuan, L.; Li, X.; Liang, T. Integrated hydraulic fracturing techniques to enhance oil recovery from tight rocks. *Pet. Explor. Dev.* **2019**, *46*, 1065–1072. [[CrossRef](#)]
- Xu, J.; Zhai, C.; Liu, S.; Qin, L.; Wu, S. Pore variation of three different metamorphic coals by multiple freezing-thawing cycles of liquid CO₂ injection for coalbed methane recovery. *Fuel* **2017**, *208*, 41–51. [[CrossRef](#)]
- Wu, Z.; Cui, C.; Jia, P.; Wang, Z.; Sui, Y. Advances and challenges in hydraulic fracturing of tight reservoirs: A critical review. *Energy Geosci.* **2022**, *3*, 427–435. [[CrossRef](#)]
- Islam, M.R. (Ed.) *Chapter 5—Reservoir Characterization of Unconventional Gas Formations*; Gulf Professional Publishing: Boston, MA, USA, 2015; pp. 237–335.
- Jia, Y.; Tsang, C.-F.; Hammar, A.; Niemi, A. Hydraulic stimulation strategies in enhanced geothermal systems (EGS): A review. *Géoméch. Geophys. Geo-Energy Geo-Resour.* **2022**, *8*, 211. [[CrossRef](#)]
- Kumari, W.; Ranjith, P.; Perera, M.; Li, X.; Li, L.; Chen, B.; Isaka, B.A.; De Silva, V. Hydraulic fracturing under high temperature and pressure conditions with micro CT applications: Geothermal energy from hot dry rocks. *Fuel* **2018**, *230*, 138–154. [[CrossRef](#)]
- Yao, J.; Deng, X.; Zhao, Y.; Han, T.; Chu, M.; Pang, J. Characteristics of tight oil in Triassic Yanchang Formation, Ordos Basin. *Pet. Explor. Dev.* **2013**, *40*, 161–169. [[CrossRef](#)]
- Guo, C.; Xu, J.; Wei, M.; Jiang, R. Experimental study and numerical simulation of hydraulic fracturing tight sandstone reservoirs. *Fuel* **2015**, *159*, 334–344. [[CrossRef](#)]
- Bukharov, D.F.; Alekseev, Y.V.; Prodan, A.S.; Nenko, A.V. Potential and Possible Technological Solutions for Field Development of Unconventional Reservoirs: Bazhenov Formation. In Proceedings of the SPE Russian Petroleum Technology Conference, Online, 26–29 October 2020. [[CrossRef](#)]
- Ipatova, A.; Chuprakov, D. Role of Preexisting Rock Discontinuities in Fracturing Fluid Leakoff and Flowback. *Transp. Porous Media* **2020**, *135*, 137–180. [[CrossRef](#)]

11. Huang, B.; Liu, J. Experimental Investigation of the Effect of Bedding Planes on Hydraulic Fracturing Under True Triaxial Stress. *Rock Mech. Rock Eng.* **2017**, *50*, 2627–2643. [CrossRef]
12. Feng, R.; Zhang, Y.; Rezagholilou, A.; Roshan, H.; Sarmadivaleh, M. Brittleness Index: From Conventional to Hydraulic Fracturing Energy Model. *Rock Mech. Rock Eng.* **2020**, *53*, 739–753. [CrossRef]
13. Li, H.; Shi, Y. Triaxial experimental investigation into the characteristics of acid-etched fractures and acid fracturing. *J. Pet. Sci. Eng.* **2021**, *202*, 108431. [CrossRef]
14. Jiang, Q.; Cui, J.; Feng, X.; Jiang, Y. Application of computerized tomographic scanning to the study of water-induced weakening of mudstone. *Bull. Eng. Geol. Environ.* **2014**, *73*, 1293–1301. [CrossRef]
15. Zhu, J.; Deng, J.; Chen, F.; Huang, Y.; Yu, Z. Water Saturation Effects on Mechanical and Fracture Behavior of Marble. *Int. J. Géoméch.* **2020**, *20*, 04020191. [CrossRef]
16. Çelik, M.Y.; Akbulut, H.; Ergül, A. Water absorption process effect on strength of Ayazini tuff, such as the uniaxial compressive strength (UCS), flexural strength and freeze and thaw effect. *Environ. Earth Sci.* **2014**, *71*, 4247–4259. [CrossRef]
17. Shakoor, A.; Barefield, E.H. Relationship between Unconfined Compressive Strength and Degree of Saturation for Selected Sandstones. *Environ. Eng. Geosci.* **2009**, *15*, 29–40. [CrossRef]
18. Zhu, J.; Deng, J.; Ma, Y.; Pak, R.Y.; Zhang, Z. Experimental study on the competing effects of strain rate and water weakening on compressive strength of saturated rocks. *Eng. Geol.* **2022**, *310*, 106873. [CrossRef]
19. Zhang, Y.; Shao, J.; Liu, Z.; Shi, C. An improved hydromechanical model for particle flow simulation of fractures in fluid-saturated rocks. *Int. J. Rock Mech. Min. Sci.* **2021**, *147*, 104870. [CrossRef]
20. Boulanouar, A.; Rahmouni, A.; Boukalouch, M.; Samaouali, A.; Géraud, Y.; Harnafi, M.; Sebbani, J. Determination of Thermal Conductivity and Porosity of Building Stone from Ultrasonic Velocity Measurements. *Geomaterials* **2013**, *3*, 138–144. [CrossRef]
21. Kassab, M.A.; Weller, A. Study on P-wave and S-wave velocity in dry and wet sandstones of Tushka region, Egypt. *Egypt. J. Pet.* **2015**, *24*, 1–11. [CrossRef]
22. Kahraman, S. The correlations between the saturated and dry P-wave velocity of rocks. *Ultrasonics* **2007**, *46*, 341–348. [CrossRef]
23. Johnston, D.H.; Toksöz, M.N.; Timur, A. Attenuation of seismic waves in dry and saturated rocks: II. Mechanisms. *Geophysics* **1979**, *44*, 691–711. [CrossRef]
24. Lockner, D. The role of acoustic emission in the study of rock fracture. *Int. J. Rock Mech. Min. Sci. Géoméch. Abstr.* **1993**, *30*, 883–899. [CrossRef]
25. Shevtsova, A.; Stanchits, S.; Bobrova, M.; Filev, E.; Borodin, S.; Stukachev, V.; Magadova, L. Laboratory Study of the Influence of Fluid Rheology on the Characteristics of Created Hydraulic Fracture. *Energies* **2022**, *15*, 3858. [CrossRef]
26. Chen, C.; Wang, S.; Lu, C.; Liu, Y.; Guo, J.; Lai, J.; Tao, L.; Wu, K.; Wen, D. Experimental study on the effectiveness of using 3D scanning and 3D engraving technology to accurately assess shale fracture conductivity. *J. Pet. Sci. Eng.* **2022**, *208*, 109493. [CrossRef]
27. Bobrova, M.; Stanchits, S.; Shevtsova, A.; Filev, E.; Stukachev, V.; Shayahmetov, T. Laboratory Investigation of Hydraulic Fracture Behavior of Unconventional Reservoir Rocks. *Geosciences* **2021**, *11*, 292. [CrossRef]
28. Maxwell, S.C.; Goodfellow, S.; Young, R.P. Acoustic Emission Geomechanics and Seismic Energy Budgets of Laboratory Hydraulic Fracturing. In Proceedings of the Geoconvention, Calgary, AB, Canada, 15–19 May 2017.
29. Bratton, T.; Canh, D.V.; Van Que, N.; Duc, N.V.; Gillespie, P.; Hunt, D.; Li, B.; Marcinew, R.; Ray, S.; Montaron, B. The nature of naturally fractured reservoirs. *Oilf. Rev.* **2006**, *18*, 4–23.
30. Nelson, R. *Geologic Analysis of Naturally Fractured Reservoirs*; Elsevier: Amsterdam, The Netherlands, 2001. [CrossRef]
31. Warpinski, N.; Teufel, L. Influence of Geologic Discontinuities on Hydraulic Fracture Propagation (includes associated papers 17011 and 17074). *J. Pet. Technol.* **1987**, *39*, 209–220. [CrossRef]
32. Li, H.; Huang, B.; Zhao, X.; Wu, Z.; Han, X.; Jiao, X.; Sun, Z. Experimental investigation on proppant transport and distribution characteristics in coal hydraulic fractures under true triaxial stresses. *J. Pet. Sci. Eng.* **2022**, *218*, 110993. [CrossRef]
33. Non-Toxic Heat Transfer Fluid MultiTherm PG-1. Physical Properties. Available online: <https://www.multitherm.com/pg-1-phys-prop.html> (accessed on 20 March 2023).
34. Kadir, A. Quick Start Guide. Available online: <https://support.einscan.com/en/support/solutions/articles/60000716595-einscan-hx-quick-start-guide> (accessed on 20 March 2023).
35. Ein Scan, H.X. Hybrid Blue Laser & LED Light Source Handheld 3D Scanner. Available online: <https://www.einscan.com/einscan-hx/> (accessed on 20 March 2023).
36. Chen, S.; Yang, C.; Wang, G. Evolution of thermal damage and permeability of Beishan granite. *Appl. Therm. Eng.* **2017**, *110*, 1533–1542. [CrossRef]
37. Li, N.; Ma, X.; Zhang, S.; Zou, Y.; Wu, S.; Li, S.; Zhang, Z.; Cao, T. Thermal Effects on the Physical and Mechanical Properties and Fracture Initiation of Laizhou Granite During Hydraulic Fracturing. *Rock Mech. Rock Eng.* **2020**, *53*, 2539–2556. [CrossRef]
38. Stanchits, S.; Burghardt, J.; Surdi, A. Hydraulic Fracturing of Heterogeneous Rock Monitored by Acoustic Emission. *Rock Mech. Rock Eng.* **2015**, *48*, 2513–2527. [CrossRef]
39. Stanchits, S.; Surdi, A.; Gathogo, P.; Edelman, E.; Suarez-Rivera, R. Onset of Hydraulic Fracture Initiation Monitored by Acoustic Emission and Volumetric Deformation Measurements. *Rock Mech. Rock Eng.* **2014**, *47*, 1521–1532. [CrossRef]
40. Zhao, K.; Ran, S.; Peng, Z.; Dao-Xue, Y.; Tian-Ye, T. Effect of moisture content on characteristic stress and acoustic emission characteristics of red sandstone. *Rock Soil Mech.* **2021**, *42*, 899–908.

41. Fortin, J.; Stanchits, S. What Can we Learn from Ultrasonic Velocities Monitoring During Hydraulic Fracturing of a Tight Shale. In Proceedings of the 49th US Rock Mechanics/Geomechanics Symposium, San Francisco, CA, USA, 28 June–1 July 2015.
42. Smith, M.B.; Bale, A.B.; Britt, L.K.; Klein, H.H.; Siebrits, E.; Dang, X. Layered Modulus Effects on Fracture Propagation, Proppant Placement, and Fracture Modeling. In Proceedings of the SPE Annual Technical Conference and Exhibition, New Orleans, LA, USA, 30 September–3 October 2001. [CrossRef]
43. Al-Nakhli, A.; Tariq, Z.; Mahmoud, M.; Abdurraheem, A. Thermochemical-Pulse Fracturing of Tight Gas: Investigation of Pulse Loading on Fracturing Behavior. In Proceedings of the SPE/IADC Middle East Drilling Technology Conference and Exhibition, Abu Dhabi, UAE, 25–27 May 2021. [CrossRef]
44. Suryadinata, M.D.; Ratnaningsih, D.R.; Ariadi, I.K.; Waliy, F.; Nugroho, W.A. Rock Mechanics Effect on Fracture Geometry and Dimensionless Fracture Conductivity of 2D Model KGD (Khristianovic-Geertsma-De Klerk) in Air Benakat Formation, Meruap Field. *Int. J. Pet. Gas Explor. Manag.* **2021**, *5*, 1–14. Available online: <https://www.eajournals.org/journals/international-journal-petroleum-gas-exploration-management-ijpgem/vol-5-issue-1-march-2021/rock-mechanics-effect-on-fracture-geometry-and-dimensionless-fracture-conductivity-of-2d-model-kgd-khristianovic-geertsma-de-kle> (accessed on 10 March 2023).
45. Yang, H.; Xie, B.; Liu, X.; Chu, X.; Ruan, J.; Luo, Y.; Yue, J. Breakdown Pressure Prediction of Tight Sandstone Horizontal Wells Based on the Mechanism Model and Multiple Linear Regression Model. *Energies* **2022**, *15*, 6944. [CrossRef]
46. Sivakugan, N.; Das, B.M.; Lovisa, J.; Patra, C.R. Determination of c and φ of rocks from indirect tensile strength and uniaxial compression tests. *Int. J. Geotech. Eng.* **2014**, *8*, 59–65. [CrossRef]
47. Singh, B.; Ranjith, P.G.; Chandrasekharam, D.; Viète, D.; Singh, H.K.; Lashin, A.; Al Arifi, N. Thermo-mechanical properties of Bundelkhand granite near Jhansi, India. *Géoméch. Geophys. Geo-Energy Geo-Resour.* **2015**, *1*, 35–53. [CrossRef]
48. Llanos, E.M.; Jeffrey, R.G.; Hillis, R.; Zhang, X. Hydraulic Fracture Propagation Through an Orthogonal Discontinuity: A Laboratory, Analytical and Numerical Study. *Rock Mech. Rock Eng.* **2017**, *50*, 2101–2118. [CrossRef]
49. Zhang, Q.; Zhang, X.-P.; Sun, W. A review of laboratory studies and theoretical analysis for the interaction mode between induced hydraulic fractures and pre-existing fractures. *J. Nat. Gas Sci. Eng.* **2021**, *86*, 103719. [CrossRef]

Disclaimer/Publisher's Note: The statements, opinions and data contained in all publications are solely those of the individual author(s) and contributor(s) and not of MDPI and/or the editor(s). MDPI and/or the editor(s) disclaim responsibility for any injury to people or property resulting from any ideas, methods, instructions or products referred to in the content.